

Electronic Theses and Dissertations, 2004-2019

2016

High Temperature Shock Tube Ignition Studies of CO₂ Diluted Mixtures

Owen Pryor
University of Central Florida

 Part of the [Aerodynamics and Fluid Mechanics Commons](#)
Find similar works at: <https://stars.library.ucf.edu/etd>
University of Central Florida Libraries <http://library.ucf.edu>

This Masters Thesis (Open Access) is brought to you for free and open access by STARS. It has been accepted for inclusion in Electronic Theses and Dissertations, 2004-2019 by an authorized administrator of STARS. For more information, please contact STARS@ucf.edu.

STARS Citation

Pryor, Owen, "High Temperature Shock Tube Ignition Studies of CO₂ Diluted Mixtures" (2016). *Electronic Theses and Dissertations, 2004-2019*. 4999.
<https://stars.library.ucf.edu/etd/4999>

HIGH TEMPERATURE SHOCK TUBE IGNITION STUDIES OF
CO₂ DILUTED MIXTURES

by

OWEN MARCUS PRYOR
B.S. University of Central Florida, 2014
B.A. University of Central Florida, 2014

A thesis submitted in partial fulfillment of the requirements
for the degree of Master of Science
in the Department of Mechanical and Aerospace Engineering
in the College of Engineering and Computer Science
at the University of Central Florida
Orlando, Florida

Spring Term
2016

© 2016 Owen Marcus Pryor

ABSTRACT

Energy demand is expected to grow by 20% over the next 10 years. In order to account for this increase in energy consumption new and novel combustion techniques are required to mitigate the effects of pollution and fossil fuel dependency. Oxy-fuel combustion in supercritical carbon dioxide (sCO₂) cycles can increase plant efficiencies up to 52% and reduce pollutants such as NO_x and CO₂ by 99%. Supercritical engine cycles have demonstrated electricity costs of \$121/MWh, which is competitive in comparison to conventional coal (\$95.60/MWh) and natural gas power plants (\$128.4/MWe). This increase in efficiency is mainly driven by the near-liquid density of the working fluid (sCO₂), in the super critical regime, before entering the turbine for energy extraction of the high pressure and high density sCO₂ gas. In addition, supercritical CO₂ engine cycles produce near-zero air emissions since CO₂, a product of combustion, is the working fluid of the system which can be regenerated to the combustor. The predictive accuracy and lack of combustion models in highly CO₂ diluted mixtures and at high pressures is one the major limitations to achieving optimum design of super critical engine combustors. Also, most natural gas mechanisms and validation experiments have been conducted at low pressures (typically less than 40 atm) and not in CO₂ diluted environment. Thus experimental data is important for the development of modern combustion systems from work focusing on supercritical carbon dioxide cycles to rotational detonation engines. This thesis presents the design of the shock tube and two optical diagnostic techniques for measuring ignition delay times and species time histories using a shock tube in CO₂ diluted mixtures.

continued

Experimental data for ignition delay times and species time-histories (CH₄) were obtained in mixtures diluted with CO₂. Experiments were performed behind reflected shockwaves from temperatures of 1200 to 2000 K for pressures ranging from 1 to 11 atm. Ignition times were obtained from emission and laser absorption measurements. Current experimental data were compared with the predictions of detailed chemical kinetic models (available from literature) that will allow for accurate design and modeling of combustion systems.

ACKNOWLEDGMENTS

This work was completed with the help of the Vasu Research Group and Dr. Subith Vasu. The work was sponsored by the University Turbines Systems Research Program, the National Energy Technology Laboratory and the Department of Energy.

TABLE OF CONTENTS

LIST OF FIGURES	x
LIST OF TABLES	xii
LIST OF EQUATIONS	xiii
CHAPTER 1: INTRODUCTION AND BACKGROUND	1
CHAPTER 2: DEVELOPMENT OF THE SHOCKTUBE.....	5
Shock tube Background	5
Derivation of the Ideal Shock Tube Equations	6
Normal Shock Equations between Region 1 and 2.....	7
Isentropic Expansion between Regions 3 and 4	8
Relating Region 2 and Region 5 through the Normal Shock Equations.....	9
Relationship between Region 1 and Region 5	11
Shock Tube Simulations	12
Simulation of the Shock Tube by KASIMIR 3.....	12
Simulations of the Shock Tube in FROSH.....	13
Experimental Setup of the Shock Tube	14
Driver Section	15
Driven and Test Sections	15

Mixing Tank.....	17
Experimental Uncertainty	17
Uncertainty in the Velocity Measurement	18
Uncertainty in the Pressure and Temperature	20
CHAPTER 3: OPTICAL DIAGNOSTOCS AND LASER SPECTROSCOPY	21
Ignition Delay Measurements.....	21
Experimental Setup.....	22
Defining the Ignition Delay Time.....	23
Introduction to Single-Species Absorption Spectroscopy	24
Beer-Lambert Law	24
Complications with Single Species Absorption Spectroscopy	25
Carbon Monoxide Species Time-histories.....	26
Experiment Setup for Carbon Monoxide Laser	26
Laser Characterization	27
Interfering Species	28
Methane Species Time-histories.....	29
Experiment Setup for Methane Laser	29
High Temperature Absorption Cross-section Measurements	30
Laser Characterization	31

Interfering Species	31
CHAPTER 4: SIMULATIONS AND MODELING	33
Effects of Pressure on Methane Ignition.....	33
Ignition Delay Times	34
Key Species Time Histories.....	35
Effect of Carbon Dioxide Dilution at Low Pressures	39
Ignition Delay Times	39
Temperature and Pressure Rise.....	40
Effect of Carbon Dioxide Dilution at High Pressures	42
Ignition Delay Times	42
Temperature and Pressure Rise.....	43
Low Fidelity of Models	45
CHAPTER 5: RESULTS AND DISCUSSIONS	46
Ignition Delay Time Measurements.....	46
Experiments at 1 atm	47
Experiments at 4 atm	51
Experiments at 8 atm	54
Ignition Delay Time Correlation.....	55
Alternative Methods for measuring the ignition delay time	56

Bifurcation of Shockwave.....	57
Other Non-idealities.....	59
CHAPTER 6: CONCLUSION	62
REFERENCES	64

LIST OF FIGURES

Figure 1: Ignition Delay Times of CH ₄ Oxidation in a CO ₂ bath gas at 20 and 300 atm.....	3
Figure 2: Image of shock tube during experiment	6
Figure 3: Figure 3: Diagram of the Shock Tube in time and space	7
Figure 4: Comparison of Kistler and PCB 5 at the end wall location.....	10
Figure 5: Schematic for the Ignition Delay Time Measurement using the 430 nm filter.....	16
Figure 6: Carbon Dioxide Spectrum and common interfering species.....	22
Figure 7: Carbon Dioxide Spectrum and common interfering species.....	26
Figure 8: Wavelength of 4.6 μm wavelength vs. the operating current	27
Figure 9: Comparison of the Spectrum of Carbon Monoxide to the Optimal Laser Output	28
Figure 10: Spectrum for Carbon Monoxide and five other common products.....	29
Figure 11: Methane Absorption Cross-section at elevated temperatures and pressures.....	30
Figure 12: Characterization of 3.4 μm laser	31
Figure 13: Mid Infrared Spectrum for Methane and other common interfering species at 296 K and 1 atm.....	32
Figure 14: Low Pressure Ignition Delay Times	34
Figure 15: High Pressure Ignition Delay Times	35
Figure 16: Effect of Pressure on Carbon Monoxide Time-histories.....	36
Figure 17: Effect of Pressure on the formation of selected radicals	38
Figure 18: Effect of Carbon Dioxide Dillution on Methane Oxidation at elevated pressures.....	40
Figure 19: Temperature and Pressure Rise at 10 atm and 1000 K.....	41

Figure 20: Effect of carbon dioxide concentration on high pressure ignition delay times.	43
Figure 21: Temperature and Pressure Time-histories at 300 atm and 1000 K	44
Figure 22: Comparison of Rise Time as a function of carbon dioxide concentration.	45
Figure 23: Comparion of time zero betwene laser and pressure traces	47
Figure 24: Comparison of ignition delay times for varying carbon dioxide mole fractions.....	50
Figure 25: Pressure and CH ₄ mole fraction time-histories during ignition.....	51
Figure 26: Ignition Delay Times at pressures around 4 atm for different equivalence ratios compared to experiments at atmospheric conditions.	53
Figure 27: Ignition delay times at 8 atm.	55
Figure 28: Comparisons of Different Methods of Ignition Delay Time Measurements.....	57
Figure 29: Example of Bifurcation of Reflected Shockwave.	58
Figure 30: Comparison of the measured pressure to the calculated pressure	60

LIST OF TABLES

Table 1: Summary of Experimental Data at Atmospheric Pressure	48
Table 2: Summary of Ignition Delay Experiments at 4 atm	52
Table 3: Summary of Ignition Delay Experiments at 8 atm.	54

LIST OF EQUATIONS

(1) Ratio of Pressures across a Normal Shockwave	8
(2) Ratio of Densities across a Normal Shockwave.....	8
(3) Ratio of Temperatures across a Normal Shockwave	8
(4) Speed of Sound.....	9
(5) Ideal Gas Law.....	9
(6) Velocity of a Shockwave.....	9
(7) Isentropic Expansion of an Expansion Wave.....	9
(8) Relationship between the Speeds of Sound in Regions 3 and 4.....	9
(9) Ratio of Temperatures between Regions 3 and 4.....	9
(10) Ratio of Pressures between Regions 3 and 4.....	9
(11) Ratio of Temperatures between Regions 1 and 4.....	9
(12) Conservation of Mass in Shock-fixed Coordinate System.....	10
(13) Conservation of Mass in Laboratory-fixed Coordinate System.....	10
(14) Velocity of Reflected Shockwave	10
(15) Velocity of Region 2 in terms of Reflected Shockwave	10
(16) Ratio of Densities between Regions 2 and 5.....	11
(17) Velocity of Region 2 in terms of Incident Shockwave	11
(18) Ratio of the Speed of Sounds	11
(19) Ratio of Pressures between Regions 2 and 5.....	11
(20) Ratio of Temperatures between Regions 2 and 5.....	11

(21) Ratio of Pressures between Regions 1 and 5.....	12
(22) Ratio of Temperatures between Regions 1 and 5.....	12
(23) Generalized Uncertainty Equation	18
(24) Equation of a Line in Slope-Intercept Form.....	18
(25) Fitness of a Line, χ^2	18
(26) Derivative of χ^2 with respect to the intercept, a	18
(27) Derivative of χ^2 with respect to the slope, b.....	18
(28) Intercept of a Line, a	19
(29) Slope of a Line, b	19
(30) The Constant Δ	19
(31) Uncertainty in the Intercept of the Line, a	19
(32) Uncertainty in the Slope of the Line, b	20
(33) Uncertainty in the End Wall Velocity.....	20
(34) Uncertainty in the Test Pressure, P5	20
(35) Uncertainty in the Test Temperature, T5	20
(36) Beer-Lambert Law	24
(37) Modified Arrhenius Equation for Ignition Delay Times.....	56
(38) Ignition Delay Time Correlation.....	56

CHAPTER 1: INTRODUCTION AND BACKGROUND

Oxy-fuel combustion is a potential solution for improving current engine technology and reducing harmful pollutants. By burning oxygen instead of air which contains nitrogen, the chemistry is reduced to carbon dioxide and water as the only products. This allows for separation of the products as water may be easily condensed and removed from the cycle completely. Once the water is removed, the carbon dioxide may be captured and stored through sequestration [1-3]. The problem with oxy-fuel combustion is that such a mixture as Fuel+O₂ is incredibly volatile and hard to control and is the reason that engines use air as the oxidizer so that the oxygen may be diluted and the reactions controlled. The solution explored in this thesis is the use of carbon dioxide as the diluent as it is already a product. This would allow for the same method of carbon dioxide isolation for sequestration and is also allows for more controlled reactions.

The next step for carbon dioxide diluted mixtures is referred to as supercritical carbon dioxide. Supercritical carbon dioxide combines the simplicity of oxy-fuel combustion with the high density of a supercritical fluid to increase the power output of the system. By operating the system at pressures between 100 atm (low pressure) and 300 atm (high pressure), the carbon dioxide will operate above its critical point of 71 atm for the duration of the cycle. According to simulations done at the Southwest Research Institute, this has the potential to increase the efficiency of the cycle to as high as 64% while maintaining zero NO_x emissions and capturing up to 99% of the carbon dioxide created [4, 5]. The cost of such a system has been shown be comparable at a price of \$121/MWh compared to conventional coal (\$96.60/MWh) or natural gas (\$128.4/MWe) [4, 6]. Two fuels are currently considered to be used in the supercritical cycle

and are explored in detail, methane and syngas. The first is the main component in natural gas and the second is a synthetic fuel created from combinations of hydrogen and carbon monoxide. Both fuels are well understood and considered to be the two most likely fuels to be used in supercritical cycles.

The problem is that there is limited information about the chemical kinetics associated with any carbon dioxide diluted mixtures, let alone mixtures at supercritical conditions. There has been several works looking at the effects of supercritical carbon dioxide on the corrosion of different materials [7-9]. These works focused on various metal alloys which could be used for combustor designs. There have also been several studies looking at the different chemical properties of the fluid including the buoyancy, transport properties and the equation of state but there has been little done on the chemical kinetics when carbon dioxide is added to the system [10-12].

The work that has been done has mainly focused on the flame speed measurements and burning rates when nitrogen is replaced with carbon dioxide [13-16]. There has also been studies looking into the chemical effects at low pressures with respect to the flammability limits and burning velocities of such mixtures [17, 18]. Until recently, there had been very little on the effects of carbon dioxide on the ignition delay times of fuels. Holton et al. looked into the effects adding small amounts of carbon dioxide (5-10%) into natural gas mixtures of methane, ethane and propane [19]. The other work on auto ignition delay times was by Vasu et al. which focused on mixtures of syngas with mole fractions of carbon dioxide as high as 24% [20]. Recently, with the focus on supercritical carbon dioxide, two papers have been published using shock tubes to look at the ignition of high carbon dioxide mixtures to pressures up to 10 atm. The first paper by

Hargis and Petersen looked into the ignition delay times of methane mixtures with increasing carbon dioxide concentrations [21]. This paper presented works on various methods to determine the ignition delay times as well as some of the added concerns with carbon dioxide but found little deviation from the predictive models. The other work by Koroglu et al., performed by the University of Central Florida, measured the ignition delay times at pressures up to 4 atm but incorporated laser absorption techniques to measure the methane time-histories during combustion in which the authors also determined that there was little deviation from the models [22].

One reason that there has been so little deviation from the models is that both the GRI 3.0 and Aramco 1.3 mechanisms, the two main chemical kinetic mechanisms for natural gas, were based off of experiments up to 10 atm [23, 24]. A comparison of these two mechanisms reveals that there is little difference between the two models at the low pressures (Figure 1).

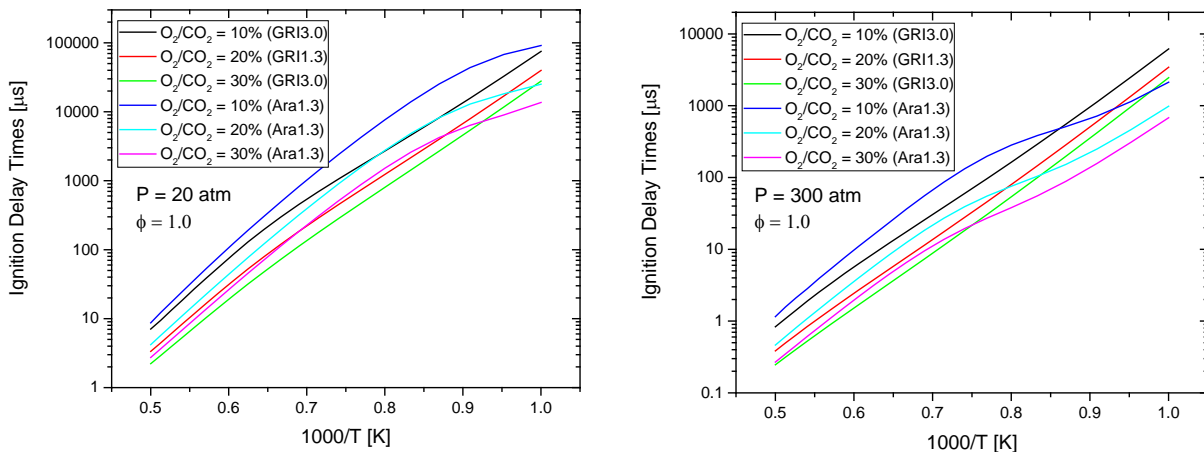


Figure 1: LEFT: Ignition Delay Times of CH₄ Oxidation in a CO₂ bath gas at 20 atm. Right: Ignition Delay Times of CH₄ Oxidation in a CO₂ bath gas at 300 atm. The two models shown above clearly show different results for the two conditions showing that there is a lack of understanding at the conditions for supercritical CO₂. ($\phi=1$).

Even at a pressure of 20 atm, the models follow a similar trend but at the pressures required for supercritical carbon dioxide, there is a major deviation in the trends between the two models. It is also concerning as neither mechanism is validated for such conditions and therefore any fluid dynamics simulation or combustor design is seriously flawed when trying to represent such conditions.

This work, although unable to extend the pressures for supercritical carbon dioxide builds on the previous work from the University of Central Florida as well as be the first to examine syngas mixtures at pressures around 10 atm using both ignition delay times and carbon monoxide time histories. This thesis describes the use of a shock tube, an ideal test facility for exploring chemical kinetics, from the conceptual theoretical ideals to the implementation of the high purity shock tube at the university and the how the shock tube deviates from the ideal. It discusses the optical diagnostics and laser absorption spectroscopy that is utilized in the experiments. The experiments are presented and explained in detail as well as several sources of uncertainty. Finally, the thesis is concluded by describing exploring several major trends further and the future work that is to be created based on these experiments.

CHAPTER 2: DEVELOPMENT OF THE SHOCKTUBE

Shock tubes are a key device for the exploration of chemical phenomenon that were studied. As a shock tube is a highly repeatable device with controllable temperatures and pressures, it was chosen for the current study.

Shock tube Background

Shock tubes utilize two sections referred to as the driven and driver sides that are separated by a thin diaphragm. By pressurizing one side of the device with an inert gas, a pressure differential is formed between the high pressure driver side and the low pressure driven side. The diaphragm is then removed and a shockwave is formed due to the pressure discontinuity between the two previously separated systems creating a pressure that is higher than the low pressure section. At the end wall, the shockwave reflects causing a second pressure increase to occur that corresponds to the maximum pressure seen during the experiment. At the same time as the creation of the shockwave, expansion waves are created that travel in the opposite direction. At the end of the experiment, the expansion waves reduce the test pressure and settle the tube at an equilibrium pressure. Figure 2 shows an example of a shock tube during the experiment.

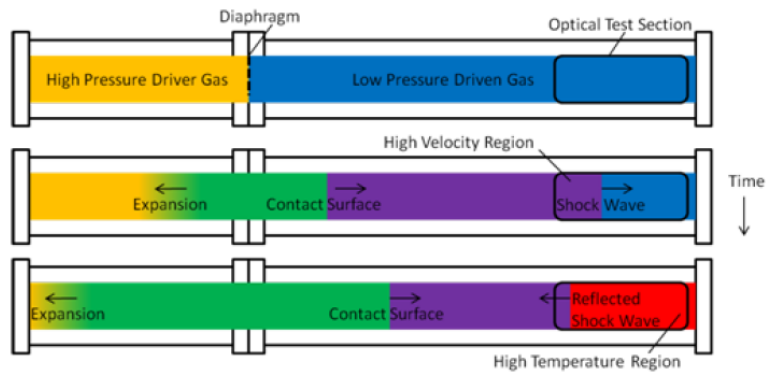


Figure 2: Image of shock tube during experiment. Top image shows tube before the diaphragm is removed. The second image shows the incident shockwave created by the pressure discontinuity. The third image shows the shockwave reflection and the high temperature test area [25].

Derivation of the Ideal Shock Tube Equations

The strength of the shockwave and the experimental conditions are controlled using the initial pressures in each section. By dividing the shock tube into five distinct regions and using the normal shockwave relations, the pressure and temperature can be mathematically determined. Region 1 is defined as the section preceding the shockwave. In Figure 1 above, it is labelled as the low pressure driven gas. The second region is defined as the section trailing the normal shockwave, or the high velocity region in Figure 1. The third region is the space between the contact surface of the driven and driver gases and the expansion waves. The fourth region is the section of high pressure gas before the experiment. The final region is the area located behind the reflected shockwave and is considered the test conditions. Figure 3 breaks down each of the five regions into the time and space coordinates for the experiment based on an x-t diagram.

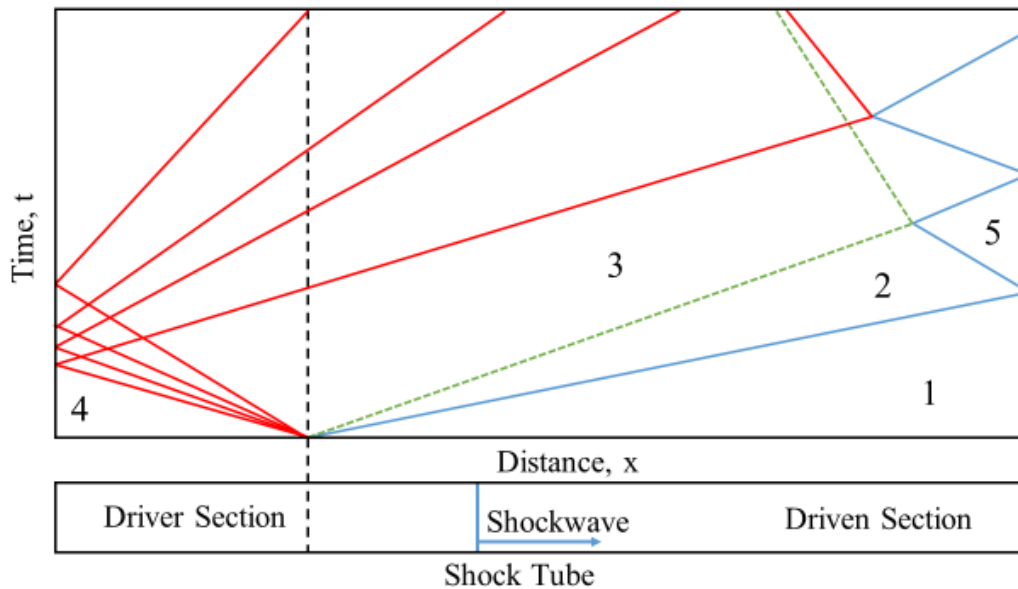


Figure 3: Diagram of the Shock Tube in time and space. Each of the regions are labeled 1-5 to correspond to the description above. Blue Lines represent shockwaves, green lines represent the contact surface between the driver and driven gases. Red lines represent expansion waves.

The derivation below, based on the work by Nishida et al. establishes the basis for both the simulations to predict the behavior of the shock tube and establishes the equations used in the uncertainty analysis of the test condition that are described later in this chapter [26].

Normal Shock Equations between Region 1 and 2

As the diaphragm is removed in an ideal shock tube, a normal shockwave is formed. Utilizing the equations derived by the Rankine-Hugoniot Conditions and the laws of conservation of mass, momentum and energy, the ratio of the pressure, density and temperature (Equations 1-3) can be determined between across the incident shockwave.

$$\frac{P_2}{P_1} = 1 + \frac{2\gamma}{\gamma + 1}(M_1^2 - 1) \quad (1)$$

$$\frac{\rho_2}{\rho_1} = \frac{(\gamma + 1)M_1^2}{(\gamma - 1)M_1^2 + 2} \quad (2)$$

$$\frac{T_2}{T_1} = 1 + \frac{2(\gamma - 1)}{(\gamma + 1)^2} \frac{\gamma M_1^2 + 1}{M_1^2} (M_1^2 - 1) \quad (3)$$

where P_x is the pressure for a given region, ρ_x is the density for a given region, T_x is the temperature for a given region, γ is the ratio of specific heat for the driven gas, and M_1 is the mach number for the incident shockwave.

Isentropic Expansion between Regions 3 and 4

By setting a particular ratio of pressures for P_4/P_1 , the Mach number for the shockwave can be determined which must be related to each other using regions 2 and 3. Regions 2 and 3 are divided by the contact surface of the gases. As the gases are moving at together and there is nothing discontinuity on the fluid field, the velocity and the pressure is constant across the contact surface (both the temperature and the density may be different). As the expansion that occurs through an isentropic process, the relationships between the temperature and the pressure can be established between regions 3 and 4. Through the isentropic relations and normal shockwave equations, the ratio for the pressure in P_4/P_1 can be derived in terms of the Mach number, and the temperatures and ratios of specific heats for the driven and driver section. (Equation 4-11). Equation 4 represents the speed of sound in an ideal gas and Equation 5 is the

Ideal Gas Law. Equation 6 is the equation for the velocity of a shockwave. Equation 7 and 8 are based on isentropic expansion and Equation 9-10 are the isentropic relations.

$$a = \sqrt{\gamma RT} \quad (4)$$

$$P = \rho RT \quad (5)$$

$$U_2 = \frac{2a_1}{\gamma_1 + 1} \left[M_s - \frac{1}{M_s} \right] \quad (6)$$

$$\frac{2a}{\gamma - 1} + U = \text{constant} \quad (7)$$

$$\frac{2}{\gamma_4 - 1} a_4 = \frac{2}{\gamma_4 - 1} a_3 + U_2 \quad (8)$$

$$\frac{T_4}{T_3} = \left(\frac{a_4}{a_3} \right)^2 \quad (9)$$

$$\frac{P_4}{P_3} = \left(\frac{a_4}{a_3} \right)^{\frac{2\gamma_4}{\gamma_4 - 1}} = \frac{P_4}{P_2} \quad (10)$$

$$\frac{P_4}{P_1} = \left(\frac{P_4}{P_2} \right) \left(\frac{P_2}{P_1} \right) = \frac{2\gamma_1 M_s^2 - (\gamma_1 - 1)}{\gamma_1 + 1} \left[1 - \frac{\gamma_4 - 1}{\gamma_1 + 1} \frac{a_1}{a_4} \left(M_s - \frac{1}{M_s} \right) \right]^{-2\gamma_4/(\gamma_4 - 1)} \quad (11)$$

Relating Region 2 and Region 5 through the Normal Shock Equations

The equations for the reflected shockwave may also be derived using the normal shock relations by considering the fifth region as the high pressure side and the lower pressure side being Region 2. Through the Conservation of Mass, the velocity on each side of the shockwave in a shock fixed coordinate system can be related to the density on either side (see Figure 4). Using the

relationships established in the two coordinate systems, the velocity from the Conservation of Mass is related to the velocity of the incident shockwave in the laboratory-fixed coordinate system (Equation 12-13).

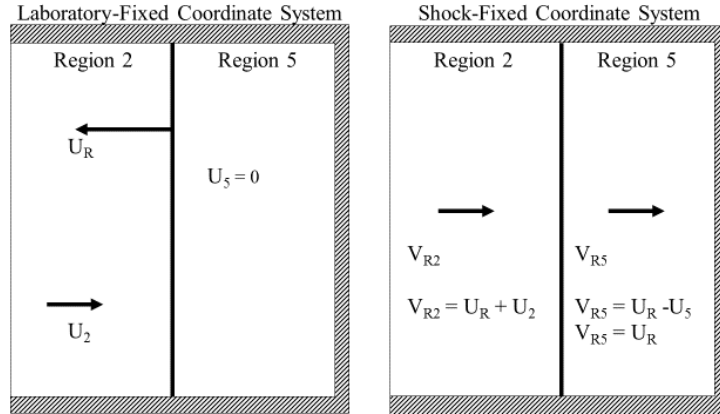


Figure 4: Two Frames of Reference for the Reflected Shock Wave. The velocities in the shock-fixed coordinate system are related to reference frame of the moving shockwave.

Manipulating the equations and substituting the equation for the reflected shockwave Equation 14), the equation for the particle velocity in Region 2 can be related to the ratio of densities over the reflected shockwave and the shock-fixed velocity in Region 2 (Equation 15). Using the ratio of densities defined by the Normal Shock Equations for Regions 2 and 5 (Equation 16), the velocity in Region 2 can be written as shown in Equation 17.

$$\rho_2 V_{R2} = \rho_5 V_{R5} \quad (12)$$

$$\rho_2 (U_R + U_2) = \rho_5 U_R \quad (13)$$

$$V_{R2} = a_2 M_R \quad (14)$$

$$(15)$$

$$U_2 = (U_R + U_2) \left[1 - \frac{\rho_2}{\rho_5} \right] = a_2 M_R \left[1 - \frac{\rho_2}{\rho_5} \right]$$

$$\frac{\rho_2}{\rho_5} = \frac{(\gamma - 1)M_R^2 + 2}{(\gamma + 1)M_R^2} \quad (16)$$

$$U_2 = \frac{2a_2}{\gamma + 1} \left[M_{R_2} - \frac{1}{M_{R_2}} \right] = \frac{2a_1}{\gamma + 1} \left[M_s - \frac{1}{M_s} \right] \quad (17)$$

Relationship between Region 1 and Region 5

The ratio of the speed of sound can then be determined by combining the Ideal Gas Law (Equation 5) and the Equation for the Speed (Equation 4) of Sound to form Equation 18. Substituting the equations into the Normal Shock Equation for the Pressure Ratio gives Equation 19 and the ratio of temperatures is created by using the Ideal Gas Law to form Equation 20. From these equations, the relationship for the pressure ratio (Equation 21) and the temperature ratio (Equation 22) can be determined.

$$\left(\frac{a_2}{a_1} \right)^2 = \frac{p_2}{p_1} \frac{\rho_1}{\rho_2} = \frac{p_2}{p_1} \left[1 + \frac{\gamma - 1}{\gamma + 1} \frac{p_2}{p_1} \right] \left[\frac{\gamma - 1}{\gamma + 1} + \frac{p_2}{p_1} \right]^{-1} \quad (18)$$

$$\frac{p_5}{p_2} = \frac{2\gamma M_{R_2}^2 - (\gamma - 1)}{\gamma + 1} = \frac{\frac{\gamma + 1}{\gamma - 1} + 2 - \frac{p_1}{p_2}}{1 + \frac{\gamma + 1}{\gamma - 1} \frac{p_1}{p_2}} \quad (19)$$

$$\frac{T_5}{T_2} = \frac{p_5}{p_2} \frac{\rho_2}{\rho_5} \quad (20)$$

$$\frac{P_5}{P_1} = \frac{P_5}{P_2} \frac{P_2}{P_1} = \left[\frac{2\gamma M_s^2 - (\gamma - 1)}{\gamma + 1} \right] \left[\frac{(3\gamma - 1)M_s^2 - 2(\gamma - 1)}{(\gamma - 1)M_s^2 + 2} \right] \quad (21)$$

$$\frac{T_5}{T_1} = \frac{T_5}{T_2} \frac{T_2}{T_1} = \frac{[2(\gamma - 1)M_s^2 + (3 - \gamma)] [(3\gamma - 1)M_s^2 - 2(\gamma - 1)]}{(\gamma + 1)^2 M_s^2} \quad (22)$$

For the above equations M_s is the Mach number for the incident shockwave and γ is the ratio of specific heats for the driven gas.

Shock Tube Simulations

The shock tube at the University of Central Florida was simulated using two different programs based on the ideal shock equations. The first program, KASIMIR 3, utilizes the above derivation to determine the ideal test conditions for a given mixture. The second program, FROSH, is focused on determining the test conditions based on a given velocity at the end wall of the shock tube.

Simulation of the Shock Tube by KASIMIR 3

The KASIMIR 3 program is capable of calculating the conditions for any given region based on the velocity of the incident shockwave and the initial driven conditions, or the conditions for both the driven and driver gases. Either of these two methods will then give you a corresponding x-t diagram similar to the one shown in Figure 2. From this diagram, several things can be determined. The first is the expected pressure and temperature in the test region (Region 5). This is important for planning the experiments and determining the initial pressure in the driven section for a given driver pressure as the rupture pressure for any given diaphragm is considered

constant. Another thing that can be determined from a KASIMIR 3 simulation is the test time. The test time is determined as the time when the pressure and temperature are at the constant T_5 and P_5 conditions. This condition occurs between the arrival of the incident shockwave at the end wall and the return of the reflected shockwave at the end wall by either an expansion wave of the contact surface. KASIMIR 3 was also used to look at the pressure at a fixed location for a given time, this could then be compared to the pressure measured during the experiment.

KASIMIR 3 has several weaknesses for applying the results to an actual experiment. The first weakness is based on the fact that the program assumes an ideal, frictionless shock tube. As a result the program often predicts higher test conditions based on a slightly faster shockwave. The other issue that occurs when using KASIMIR is the relatively limited amount of gases and mixtures that are prebuilt into the program. The program only has about 15-20 gas files that are loaded into the program and almost any mixture must be created in a custom gas file which the information for can be difficult to determine. This leads to errors in the simulated values for the temperature and pressure between 150 K and 0.5 Atm at the highest conditions.

Simulations of the Shock Tube in FROSH

The frozen shock tube calculator, or FROSH, utilizes the velocity of the shockwave to calculate the test conditions behind the incident shockwave and the reflected shockwave. This is done using several different methods including prescribed velocity measurement or a measured time intervals to determine the velocity at several points before the test section given by the geometry of the shock tube. This last method is the most common use for FROSH as it incorporates the

frictional velocity losses as the shockwave travels along the driven section. The velocity of the end wall is measured using a linear regression analysis among these different points and extrapolating to the end wall location set by the user. Before the velocity can be calculated, the mixture composition and the temperature of the driven section must be inputted into the system. It then calculates the test conditions using the ideal shock equations based on the velocity calculated by the end wall.

For the experiments presented in this thesis and for most practical mixtures, FROSH is often more robust based on the method for calculating the mixture based effects as it determines the mixture properties based on the NASA polynomials. This information is much easier to determine and add to the thermodynamic database compared to the custom gas files created with KASIMIR. The use of actual data to determine the velocity is also more accurate as incorporates frictional losses from the experiment in determining the test conditions although it still is based on the ideal shock equations that often underestimate the temperature and pressure due to non-idealities present in the experiments.

Experimental Setup of the Shock Tube

The shock tube at the University of Central Florida is divided into three sections in this thesis [22, 27, 28]. The shock tube consists of a 14 cm diameter stainless steel tube with a 4.84 m long driver section and an 8.54 m driven section. The driver and driven sections are separated by a sheet of 8010 Lexan of various thicknesses. As the driver section is filled, the diaphragm flexes towards the low pressure in the driven section as the forces become unbalanced based on the

pressure difference. Eventually, the diaphragm pushes on a blade made of steel that ruptures the diaphragm into four equal petals. This allows for the breaking pressure to be controlled through a combination of diaphragm thickness and cutter position.

Driver Section

The driver section utilized mass flow controllers (Teledyne-Hastings HFC-D-303) for uniform filling for each individual experiments. The driver side pressure was monitored using an Omega PX409-1.0KAV5 static pressure transducer. Before each experiment the driver section is vacuumed using an Agilent DS102 mechanical vacuum pump.

Driven and Test Sections

Measurements for the initial pressure and temperature were performed in the driven section of the shock tube as well as the filling and vacuuming for the driven and test sections.

Before each experiment, the driven section was routinely vacuumed below 100 μ torr using a combination of a second Agilent DS102 vacuum pump and a turbo molecular vacuum pump (Agilent V301). The pressure was measured using a combination of a Lesker KJL275804LL convection gauge and a Lesker KJLC354491YF Ionization gauge with ranges between 10^{-3} torr to 1000 torr and 10^{-9} to 5×10^{-2} torr, respectively. The temperature before each experiment is measured using a T-type thermocouple. The pressure is measured using two MKS baratrons (E27D, accuracy of 0.12% of reading, and 628D, accuracy of 0.25% of reading) with ranges of

100 and 10,000 torr, respectively. The leak rate for the shock tube was measured to be 2×10^{-5} torr/min.

During the experiment, the velocity of the shock tube is measured using a five PCB 113B26 pressure transducers connected to four timer counters (Agilent 53220A) to measure the interval of time it takes for the shockwave to travel a set distance. Each of the PCBs were connected to a signal conditioner that focused the range between 0-50 psi. A Kistler 603B1 dynamic pressure transducer was placed two centimeters from the end wall opposite of the last PCB transducer. The Kistler was coated with RTV silicone to remove fluctuations caused by the temperature rise.

As a check on the system, the pressure measured by the Kistler was compared to the PCB at the same location. Figure 5 shows the comparison of the two pressure transducers at the same location and the KASIMIR 3 simulation.

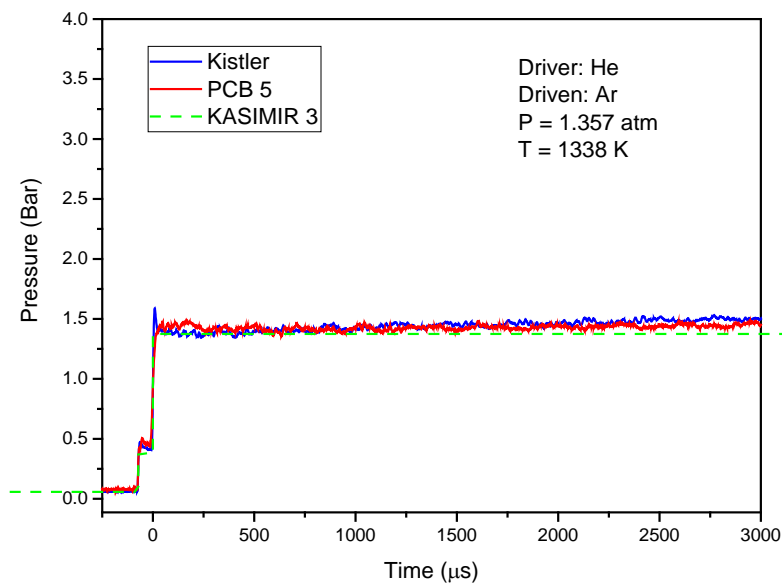


Figure 5: Comparison of Kistler and PCB 5 at the end wall location. Both values are compared to the KASIMIR 3

simulation for the calculated velocity.

Mixing Tank

A 33 L mixing tank is used to prepare all mixtures before the experiments. The mixing tank is attached to a manifold that allows for its filling into the shock tube and monitoring the pressure from the baratrons. The mixing tank utilizes a mechanical stirrer to induce turbulent mixing and allow for more homogeneous mixtures. Before a mixture is prepared, the mixing tank is vacuumed using the turbo-molecular pump overnight to ensure the accuracy of the mixture.

Helium (99.995% from Praxair) was used as the driver gas. Research grade gases of Argon (99.999%), oxygen (99.999%), carbon dioxide (99.999%) and methane (99.99%) were used for the driven gases (from Air Liquide).

Experimental Uncertainty

The uncertainty in the temperature and pressure in Region 5 can be determined using a linear regression analysis for the velocity and Equations 21-22 [29]. It was determined through experimentation that the uncertainty in each of the timer counters was 1.36 μs . The uncertainty in the position of each PCB positions was determined to be 0.25 mm based on the manufacturing specifications and the uncertainty in the end wall position was 0.125 mm. The uncertainty in the P_1 measurement was determined to be 1.3×10^{-5} Atm and the uncertainty in T_1 was determined to be 0.5 K. The uncertainty in the velocity, pressure and temperature can then be determined using the general form of the uncertainty equation (Equation 23).

$$\sigma_y^2 = \sum \left[\sigma_{x_i}^2 \left(\frac{\partial y}{\partial x_i} \right)^2 \right] \quad (23)$$

Uncertainty in the Velocity Measurement

A linear regression analysis was performed using the method of least squares[29]. This method creates a line to minimize the error between all the points in the form of:

$$y(x) = a + bx \quad (24)$$

By maximizing the probability of observing the measurements (in this case velocities) for a given standard deviation, σ_i , and minimizing the error between the measured values and a line, the fitness of a line can be determined (Equation 25).

$$\chi^2 = \sum \left[\frac{y_i - y(x_i)}{\sigma_i} \right]^2 = \sum \left[\frac{1}{\sigma_i} (y_i - a - bx_i) \right]^2 \quad (25)$$

The optimal fit for the line is then determined to be the values of a and b that minimize the weighted sum of the squares of the deviations, χ^2 . In order to minimize the value for χ^2 , the partial derivatives Equations 26-27) with the respect to a and b must be set to zero.

$$\frac{\partial}{\partial a} \chi^2 = -2 \sum \left[\frac{1}{\sigma_i^2} (y_i - a - bx_i) \right] \quad (26)$$

$$\frac{\partial}{\partial b} \chi^2 = -2 \sum \left[\frac{1}{\sigma_i^2} (y_i - a - bx_i) x_i \right] \quad (27)$$

The equations can be rewritten in terms of two simultaneous equations and the values for a and b can be solved in matrix form using the determinants as shown in Equations 28-30.

$$a = \frac{1}{\Delta} \begin{vmatrix} \sum \frac{y_i}{\sigma_i^2} & \sum \frac{x_i}{\sigma_i^2} \\ \sum \frac{x_i y_i}{\sigma_i^2} & \sum \frac{x_i^2}{\sigma_i^2} \end{vmatrix} = \frac{1}{\Delta} \left(\sum \frac{x_i^2}{\sigma_i^2} \sum \frac{y_i}{\sigma_i^2} - \sum \frac{x_i}{\sigma_i^2} \sum \frac{x_i y_i}{\sigma_i^2} \right) \quad (28)$$

$$b = \frac{1}{\Delta} \begin{vmatrix} \sum \frac{1}{\sigma_i^2} & \sum \frac{y_i}{\sigma_i^2} \\ \sum \frac{x_i}{\sigma_i^2} & \sum \frac{x_i y_i}{\sigma_i^2} \end{vmatrix} = \frac{1}{\Delta} \left(\sum \frac{1}{\sigma_i^2} \sum \frac{x_i y_i}{\sigma_i^2} - \sum \frac{x_i}{\sigma_i^2} \sum \frac{y_i}{\sigma_i^2} \right) \quad (29)$$

$$\Delta = \begin{vmatrix} \sum \frac{1}{\sigma_i^2} & \sum \frac{x_i}{\sigma_i^2} \\ \sum \frac{x_i}{\sigma_i^2} & \sum \frac{x_i^2}{\sigma_i^2} \end{vmatrix} = \sum \frac{1}{\sigma_i^2} \sum \frac{x_i^2}{\sigma_i^2} - \left(\sum \frac{x_i}{\sigma_i^2} \right)^2 \quad (30)$$

Using this method, the equation for the line can be determined and the velocity of the end wall can be calculated by assuming that the velocity is the dependent variable y and the distance from the end wall is the independent variable x.

To calculate the uncertainty in the end wall velocity, the partial derivative of the slope and intercept must be determined with respect to y. Combining this with the general form of the uncertainty equation that is shown in Equation 23, the uncertainty in the slope, b, and the intercept, a, may be determined (Equations 31 and 32)

$$\sigma_a^2 = \frac{1}{\Delta} \sum \frac{x_i^2}{\sigma_i^2} \quad (31)$$

$$\sigma_b^2 = \frac{1}{\Delta} \sum \frac{1}{\sigma_i^2} \quad (32)$$

Assuming that the velocity is decreasing in a linear relationship with the distance travelled and using the method for least squares described above the uncertainty of the end wall velocity is determined by Equation 33.

$$\sigma_{v_{endwall}}^2 = \sum \left[\sigma_{x_i}^2 \left(\frac{\partial y}{\partial x_i} \right)^2 \right] = \sigma_a^2 + \sigma_b^2 x_{endwall}^2 + \sigma_{x_{endwall}}^2 b^2 \quad (33)$$

Uncertainty in the Pressure and Temperature

After calculating the uncertainty of the end wall velocity, the pressure and velocity can be determined using the uncertainty equation using Equation 21 and 22. These equations are shown below in Equations 34 and 35.

$$\sigma_{P_5}^2 = \sigma_{v_{endwall}}^2 \left(\frac{\partial P_5}{\partial V_{endwall}} \right)^2 + \sigma_{T_1}^2 \left(\frac{\partial P_5}{\partial T_1} \right)^2 + \sigma_{P_1}^2 \left(\frac{\partial P_5}{\partial P_1} \right)^2 \quad (34)$$

$$\sigma_{T_5}^2 = \sigma_{v_{endwall}}^2 \left(\frac{\partial T_5}{\partial V_{endwall}} \right)^2 + \sigma_{T_1}^2 \left(\frac{\partial T_5}{\partial T_1} \right)^2 \quad (35)$$

The values for the uncertainty were then calculated and divided by the calculated value to get a percent error. The average error for the velocity at the end wall was less than 1% for all the tests performed. The error in the temperature and pressure was found to be less than 2% for all the experiments. The fitness of the line was also calculated for all of the experiments to determine how accurate a representation of a line was measured and this value was determined to be less than 2 for all experiments.

CHAPTER 3: OPTICAL DIAGNOSTICS AND LASER SPECTROSCOPY

This thesis covers two methods utilized to examine chemical kinetics behind reflected shockwaves. The first measurement that is performed is the measuring the auto-ignition delay time, or the time interval it takes for a combustible mixture to ignite after reaching a certain temperature and pressure, using the pressure and emissions. The second technique is the measurement of single species over the course of the experiment using laser absorption spectroscopy.

Ignition Delay Measurements

Ignition delay times are considered a vital characteristic in the development of engines. Whether it is to optimize the compression timing in a Diesel Cycle or ensuring that auto-ignition does not occur in an Otto Cycle, every fuel must have its auto-ignition characteristics mapped out.

To understand the environment that is occurring during combustion, the ignition delay time is an important characteristic that needs to be understood for a given mixture. The ignition delay time, as defined in this thesis, is the time between the pressure and temperature arriving at a certain condition and the start of the ignition. As such, a shock tube is an ideal facility for the measurement of ignition delay times due to the constant conditions after the reflected shockwave and the controllability and repeatability of the experiments.

Experimental Setup

The setup used for this thesis combines pressure measurements from the Kistler pressure transducer with optical measurements of the light emissions. A GaP trans-impedance amplified detector (Thorlabs PDA25K) with a wavelength range between 150 and 550 nm. This was used in conjunction with either a 310 nm bandpass filter with a FWHM of 10 nm (OH*), a 430 nm bandpass filter with a FWHM of 10 nm (CH*), or neither to measure the whole range of light. The determination for the filter was based on the overall signal to noise ratio of the emissions peak with preference to either filter as it reduced the rise time and therefore increased the accuracy of the measurement. In order to reduce the temporal width of the measurement, a variable slit was placed in front of the detector. Figure 6 shows a schematic of the setup for the ignition delay times.

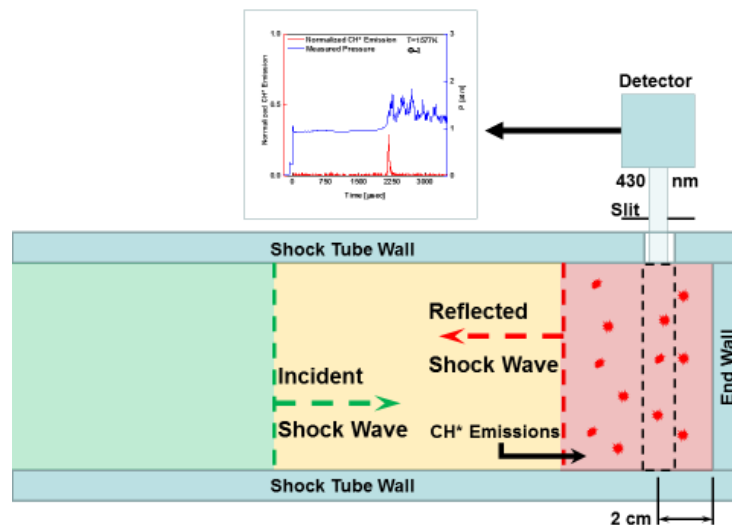


Figure 6: Schematic for the Ignition Delay Time Measurement using the 430 nm filter. The graph shows the pressure (blue) and the CH* emissions for a sample experiment (red) [27].

Defining the Ignition Delay Time

Measuring the ignition delay times of a mixture is a relatively simple experiment but there is still a large discussion on the actual definition of the ignition delay time with respect to the pressure and emissions traces.

The ignition delay time is considered to be the start of ignition but there are several possible meanings for this. One common method for measuring the ignition delay time is to trace the emissions peak back to the baseline from the point from the location of the greatest slope. This method makes sense since the traditional definition of ignition delay is to the start of ignition but it often leads discrepancies between researchers between the locations of such a point. Another method is to measure the ignition delay times as the midpoint of the emissions peak as for the start with the pressure trace. By normalizing the emissions as was done above, individual researchers are able to analyze the data in the same method and eliminate a possible source of human error. The issue with this method is it does not match either of two broadly accepted definitions of ignition with either the start of radical build up or the sufficient radical buildup to propagate the reactions. In this thesis, the value for determining the ignition delay times was chosen as the peak of the emissions trace. This value was chosen for several reasons. The first two reasons are laid out above with the elimination of error through normalization and a broadly accepted definition. The other reason is that this method for determining the ignition delay times also matched the ignition delay times as measured by the methane laser. Ignition is considered to

have occurred when the parent fuel, in this case methane, is completely depleted and the peak emissions matched closely with this determination.

Introduction to Single-Species Absorption Spectroscopy

Although ignition delay times are an important parameter for validating mechanisms, single-species absorption spectroscopy allows for further analysis of the combustion phenomenon by looking at the time-history of a single species during the experiment.

Beer-Lambert Law

Every molecule emits and absorbs light at characteristic wavelengths based on the vibrational frequencies of the chemical bonds. Each overall spectrum for any species is unique. By determining a wavelength where a given species absorbs, the concentration of a species can be related to the absorption based on the Beer-Lambert Law (Equation 36):

$$\alpha = -\ln\left(\frac{I_{tr}}{I_{ref}}\right) = \sigma(\nu, T, P) \frac{P_{tot}}{RT} \chi L \quad (36)$$

where P is the pressure in atmospheres, T is the temperature in K, R is the specific gas constant, L is the optical path length in cm, χ is the mole fraction of the absorbing species, σ is the absorption cross section in $\text{cm}^2/\text{molecule}$, I_{tr} and I_{ref} are the intensity of the laser transmitted and at a reference, and α is the absorbance, respectively. Using this equation, the species concentration can be determined as long as the pressure, temperature and absorption cross-section are known.

Complications with Single Species Absorption Spectroscopy

There are several issues that occur when using lasers to measure the concentration of a species during combustion based on the pressure, temperature and gas composition.

The first issue is that the absorption cross-section lessens at higher temperatures. This means that not only does the value change from the standard temperature and pressure but the overall absorption is reduced making it difficult to measure. This issue can be easily overcome through the use of a shock tube by measuring a known quantity of the target species at the desired temperature.

The second issue is pressure broadening. As the pressure is increased, the peaks of different species widen as shown below in Figure 7. This causes issues with combustion experiments as they are often taken at higher pressures and therefore the wavelength for any individual species must be chosen with care to avoid interference from other species.

The last major concern for single species absorption is interference from other species. As a wavelength cannot always be chosen that is isolated from all other species, interference can make it extremely difficult to measure the concentrations with any accuracy. A method to improve the technique has been developed referred to as the peak-valley scheme. In this technique, two wavelengths are chosen for a given species that have large differences in the absorption properties but little difference for other species. Using this method two measurements can be taken to remove the interference by canceling out their contributions. As long as the

interfering species absorption cross-sections due not change at both the peak and valley locations, this technique can greatly improve the accuracy of the data.

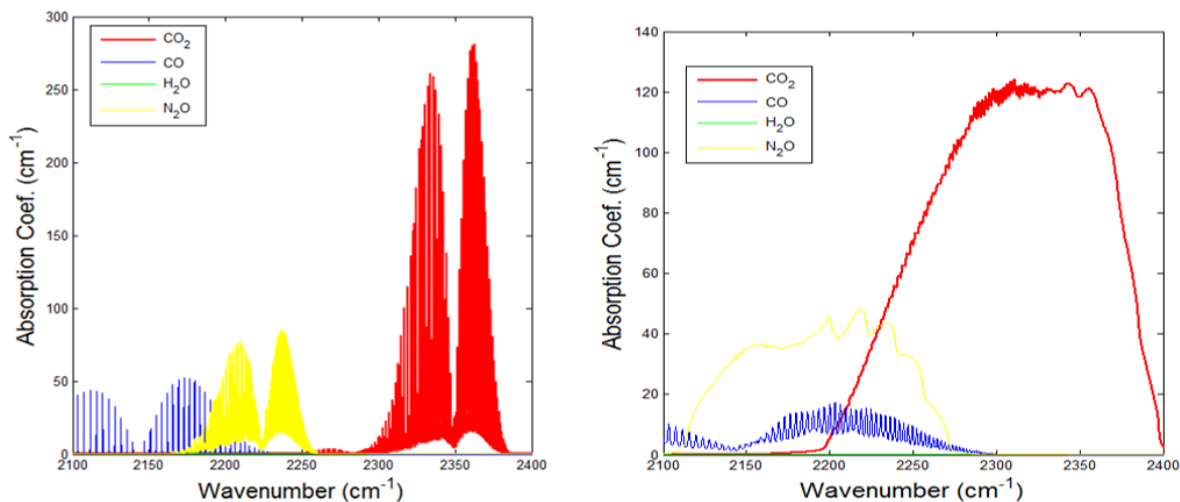


Figure 7: Carbon Dioxide Spectrum and common interfering species. LEFT: $T = 296\text{K}$ and $P = 1\text{ atm}$. RIGHT: $T = 1500\text{ K}$ and 40 atm . The spectrums on the right show much lower overall absorption coefficients but broader spectrums as well showing that at high temperatures and pressures, interference becomes a greater concern.

Carbon Monoxide Species Time-histories

Carbon monoxide is a product that is formed in nearly all combustion events. As a result, it is one of the most important species to measure for accurate chemical kinetic models. As the spectrum of carbon monoxide shows high absorbance features around $4.6\text{ }\mu\text{m}$, the carbon monoxide absorption scheme was focused around that region.

Experiment Setup for Carbon Monoxide Laser

For this thesis, a quantum cascade laser was purchased with an output of approximately 20 mW at $4.6\text{ }\mu\text{m}$ from Thorlabs (QD4580CM1) attached to a LDMC20 laser mount, also, from

Thorlabs. The laser is controlled using a current and temperature controller from Thorlabs (ITC4005). The laser is shined onto two different detectors (VIGO Optics) after traveling through a 50-50 beam splitter. The windows on the shock tube are made of sapphire glass and have a diameter of 0.6 in. After traveling through the shock tube, the laser passes through a neutral density filter, iris and bandpass filter to eliminate any interference and IR emissions.

Laser Characterization

In order to use the laser, it was characterized using a Bristol 771 Wave Meter based on its temperature and pressure. Using this the optimal spectral output was determined for the laser for maximum absorption. Figure 8 shows the wavelength of the laser for different operating currents for three different temperatures.

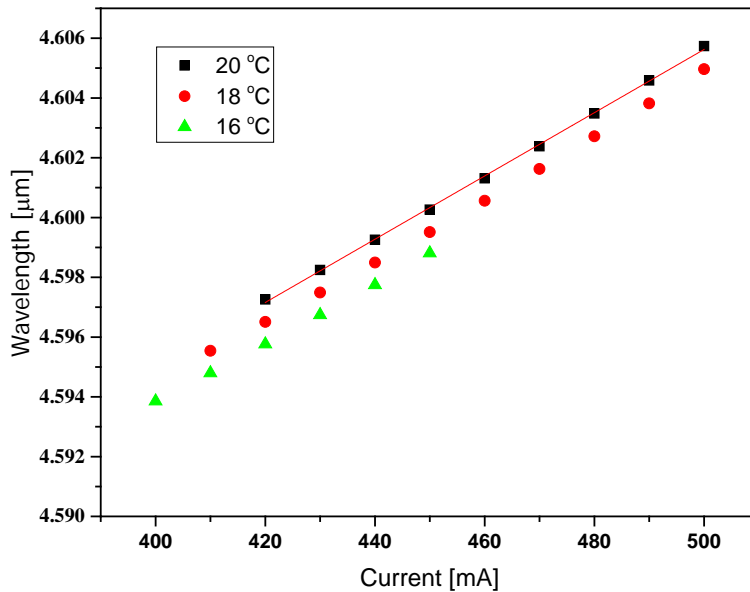


Figure 8: Wavelength of 4.6 μm wavelength vs. the operating current for three different temperatures

This data was then compared to the spectrum of carbon monoxide in this wavelength range to determine the optimal operating conditions for the laser as shown in Figure 9. It was determined through analysis that the optimal conditions for the laser was 450 mA at 20 °C.

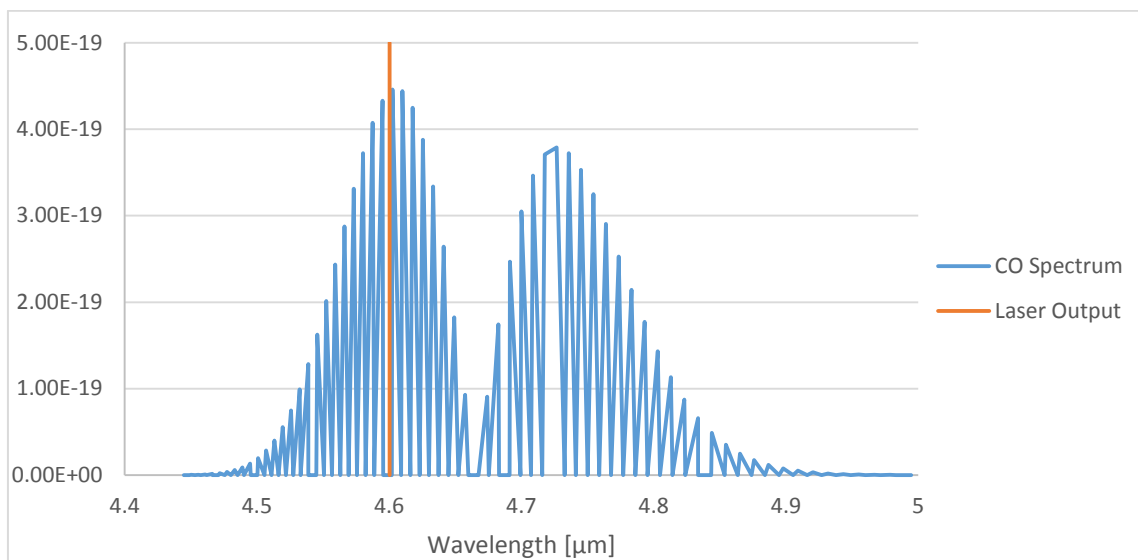


Figure 9: Comparison of the Spectrum of Carbon Monoxide to the Optimal Laser Output.

Interfering Species

Once the optimal laser settings were determined, the interference from other species were determined using Chemkin Pro for various mixtures. It was determined that due to the high absorbance characteristics resulting from the carbon oxygen triple bond, there was little absorbance at the wavelength being studied when examined at standard temperature and pressure. Figure 10 compares the five most common products during CO₂ diluted methane combustion with carbon monoxide. It shows that the species with the highest absorption in this area is water and acetylene both which are several orders of magnitude smaller than the absorption of methane.

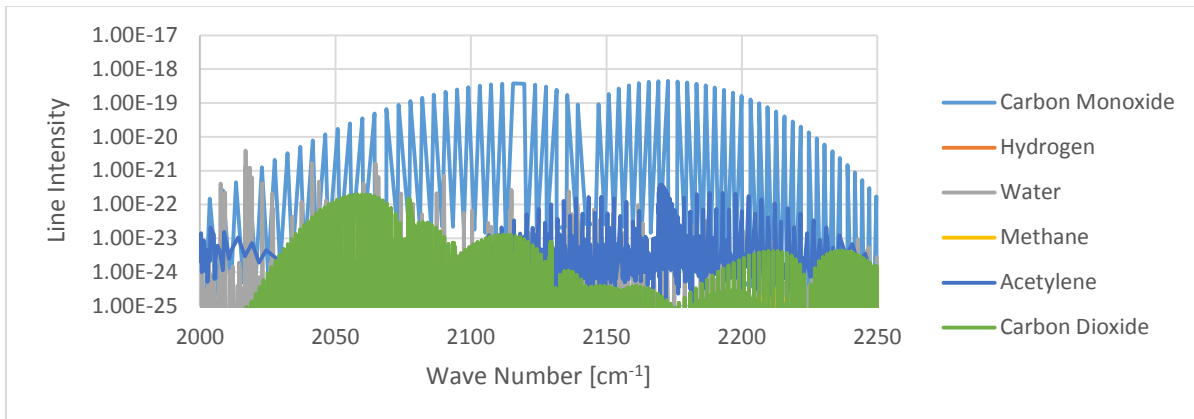


Figure 10: Spectrum for Carbon Monoxide and five other common products. There is little interference at this wavelength due to the much lower absorption cross-sections in this region.

Methane Species Time-histories

A second laser was also set up to measure the methane time-histories during combustion. This laser was used to validate the ignition delay measurements by showing the time it takes for methane to be depleted compared to the peak ignition delay measurement.

Experiment Setup for Methane Laser

The methane laser is based on the work described by Pyun et al. [30-32]. This method uses a Nanoplus DFB ICL at a wavelength of 3403.4 nm. Using this laser the methane laser can access both the P(8) line and a valley measurement for the peak-valley scheme [33].

The laser is collimated using a collimation lens from Thorlabs (C036TMEE) and mounted to a heat sink (Nanoplus TO66 Mount) [22]. A temperature controller (Thorlabs TLD001) and current controller (Thorlabs TTC001) were used with the laser. The beam was split into two

different beams using a beam splitter and shined onto two thermoelectrically cooled photodetectors from Vigo Systems (PVI-2TE-3.4).

High Temperature Absorption Cross-section Measurements

As pressures and temperatures increase, the absorption characteristics for a given species change. Experiments were performed at the same temperatures and pressures for the methane laser to measure the absorption cross-section at these engine-like conditions. These measurements, shown in Figure 11, demonstrate the effect that temperature plays on the absorption characteristics and the effect that carbon dioxide has on the absorption cross-section. From these experiments, the absorption cross-section can be determined and quantitative methane concentrations can be determined.

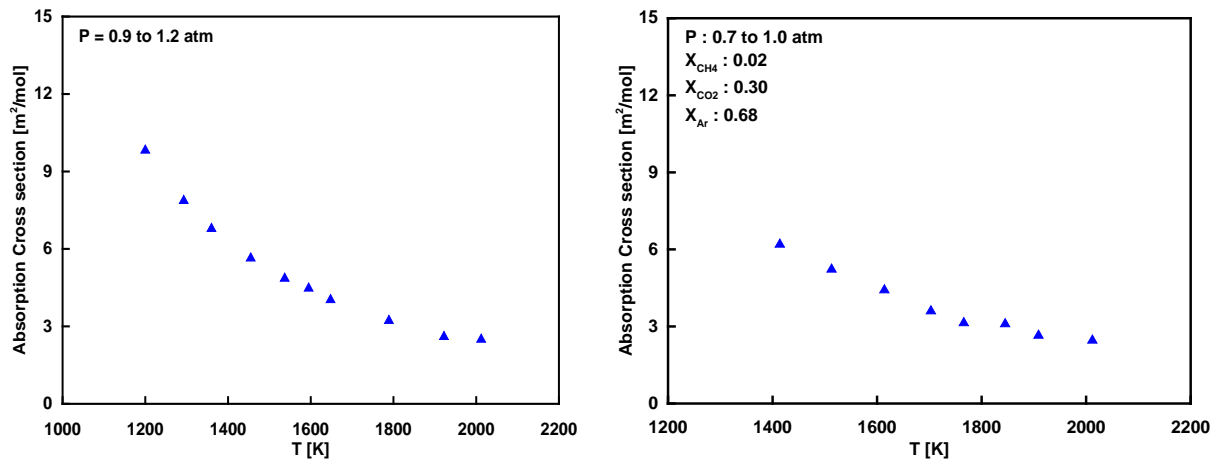


Figure 11: LEFT: Methane absorption cross-section between 1200 – 2000 K and 0.9 to 1.2 atm. A mixture of 2% methane in argon was utilized. RIGHT: Methane absorption cross-section between 1400-2000 K and 0.7 – 1.0 atm. A mixture of 2% methane and 30% carbon dioxide in argon was used. The methane absorption shows less absorption with the addition of carbon dioxide at the lower temperatures but approximately the same value around 2000 K. This shows that the addition for carbon dioxide must be accounted for during experiments for

accurate measurements. Figures taken from Koroglu et al. [22].

Laser Characterization

In order to verify the wavelength for the laser, the spectrum was measured with a wave meter (Bristol 771) in the same method as the 4.6 μm laser. Figure 12 shows the wavelength of the laser at different current levels for a set temperature. This could then be compared to the spectrum at atmospheric conditions and determine the optimal set points for both the peak and valley measurements.

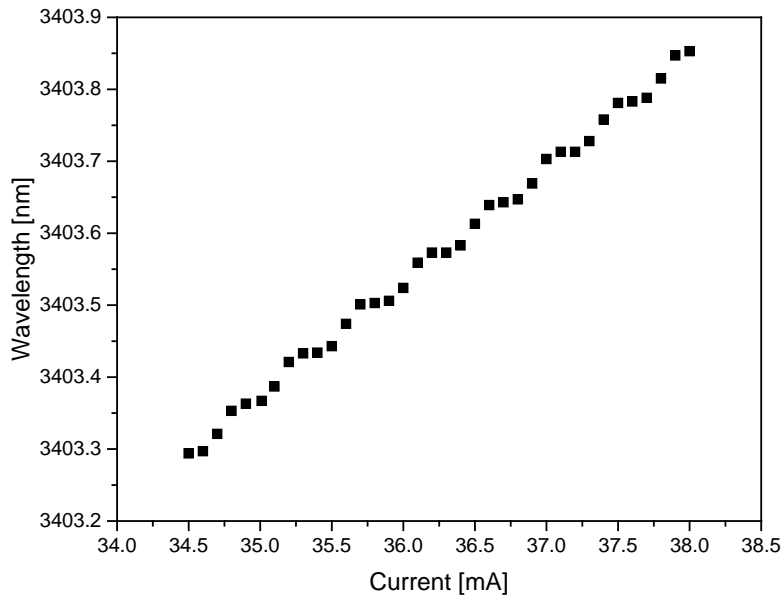


Figure 12: Characterization of 3.4 μm laser at 9.62 k Ω .

Interfering Species

A peak-valley absorption scheme was used to measure methane concentrations due to the high interference of other species in the wavelength. The valley measurement was done to eliminate

these species as the absorption remained relatively constant throughout the wavelength range of the laser. Figure 13 shows the methane spectrum and other common species that absorb in the vicinity of the P(8) band.

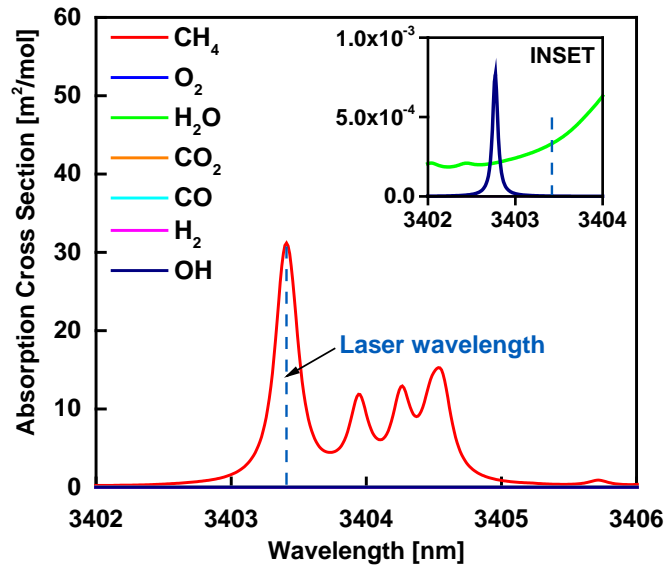


Figure 13: Mid Infrared Spectrum for Methane and other common interfering species at 296 K and 1 atm [22].

CHAPTER 4: SIMULATIONS AND MODELING

Simulations of combustors are a common design tool for any gas turbine or engine. Through the use of multistep mechanisms such as the GRI 3.0 and Aramco 1.3, accurate predictions can be made about the combustion environment through computational fluid dynamics [23, 24]. In order for these simulations to be accurate, however, the combustion mechanisms that determine the species concentrations, temperature rises, etc. may have thousands of reactions and hundreds of species with rates that control which reactions dominate at any given condition. Therefore, chemical kinetic mechanisms must have been validated over the range of conditions using experimental data.

Throughout the chapter, two common natural gas mechanisms that have been well validated will be used to model the effects that pressure and carbon dioxide dilution have on the combustion of methane. This chapter will discuss the ignition delay times for these mixtures as well as key species that play a vital role in the reactions. All of the modeling was done using the Chemkin Pro software in a homogeneous batch reactor.

Effects of Pressure on Methane Ignition

In order to establish a baseline, methane oxidation was modeled without any carbon dioxide dilution. The pressures explored for these reactions were between 1 and 300 atm to cover the full range between atmospheric pressure and standard gas turbine operation to the considered set point for direct-fired supercritical carbon dioxide cycles.

Ignition Delay Times

Both models show relatively good agreement with each other for these conditions which is not surprising as it is still close to the range of pressures that the mechanisms are validated for. The main difference between the mechanisms is the higher rise initial rise at the high temperatures and the tapering off at lower temperatures for the Aramco mechanism. Aramco is predicting slight change in the major reactions at the higher pressures resulting in a change in the activation energy of the system. One interesting thing to note is that both mechanisms end around the same value at a temperature of 1000 K. Figure 14 shows the ignition delay times at low temperatures.

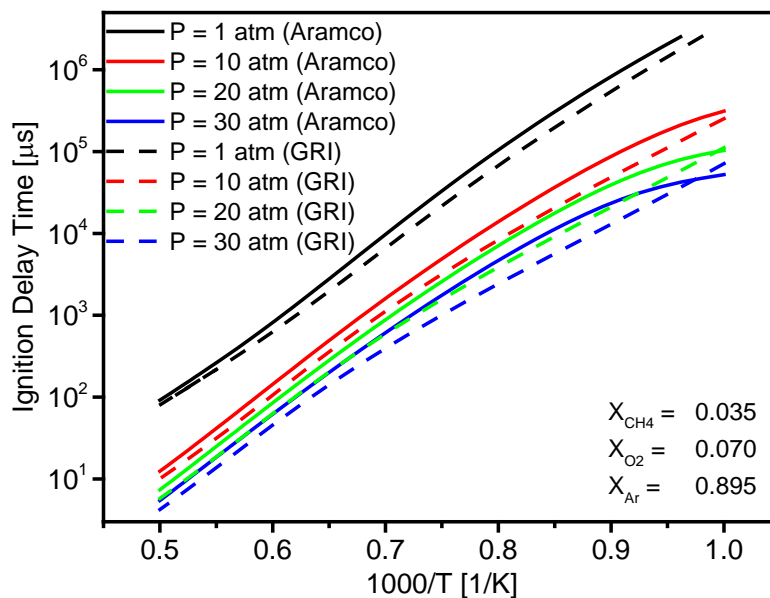


Figure 14: Low Pressure Ignition Delay Times. Aramco 1.3 is shown as solid lines and GRI 3.0 as dashed.

At higher pressures the ignition delay time drops even further and start to deviate between the two models. The GRI 3.0 mechanism continues to show a simple logarithmic behavior and seem to have mainly vertical shifts between the different pressure levels. The Aramco mechanism shows much more interesting trends though. The change around 1100 K where the dominant

reactions changes is much more pronounced compared to the lower pressures. It is clear that by at the most important pressures for supercritical carbon dioxide, there is little consensus on how the mixtures will adapt to the high pressures and this is before carbon dioxide has been added to the mixture. Figure 15 shows the ignition delay times of methane oxidation at elevated pressures.

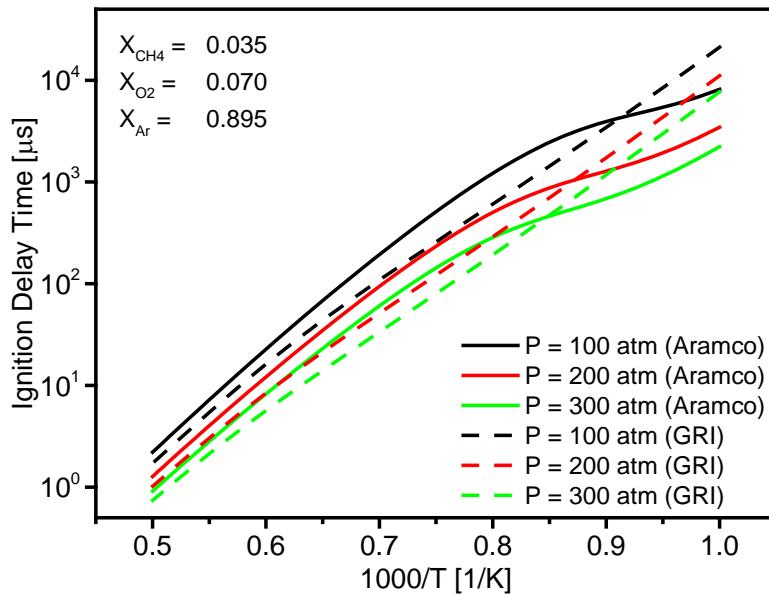


Figure 15: High Pressure Ignition Delay Times. Aramco 1.3 is shown as solid lines and GRI 3.0 as dashed.

Key Species Time Histories

One major species that is a concern is the toxic gas carbon monoxide. Carbon monoxide is a pollutant as well as being fatal at low concentrations and is one of the targets for reduction by organizations such as the EPA. According to the models, the overall carbon monoxide creation is independent of pressure. Both models show agreement with each other except for the position of the peak which is a function of ignition delay time. The top of Figure 3 shows the amount of carbon monoxide formed in a mixture of methane and oxygen with an equivalence ratio of 1.

Carbon dioxide shows the same trends carbon monoxide in terms of pressure and temperature for both models. The carbon dioxide concentration increases to a level and then steadies after combustion. Again, the different rise times is a result of different ignition delay times between the models. The bottom of Figure 16 shows the carbon dioxide time histories.

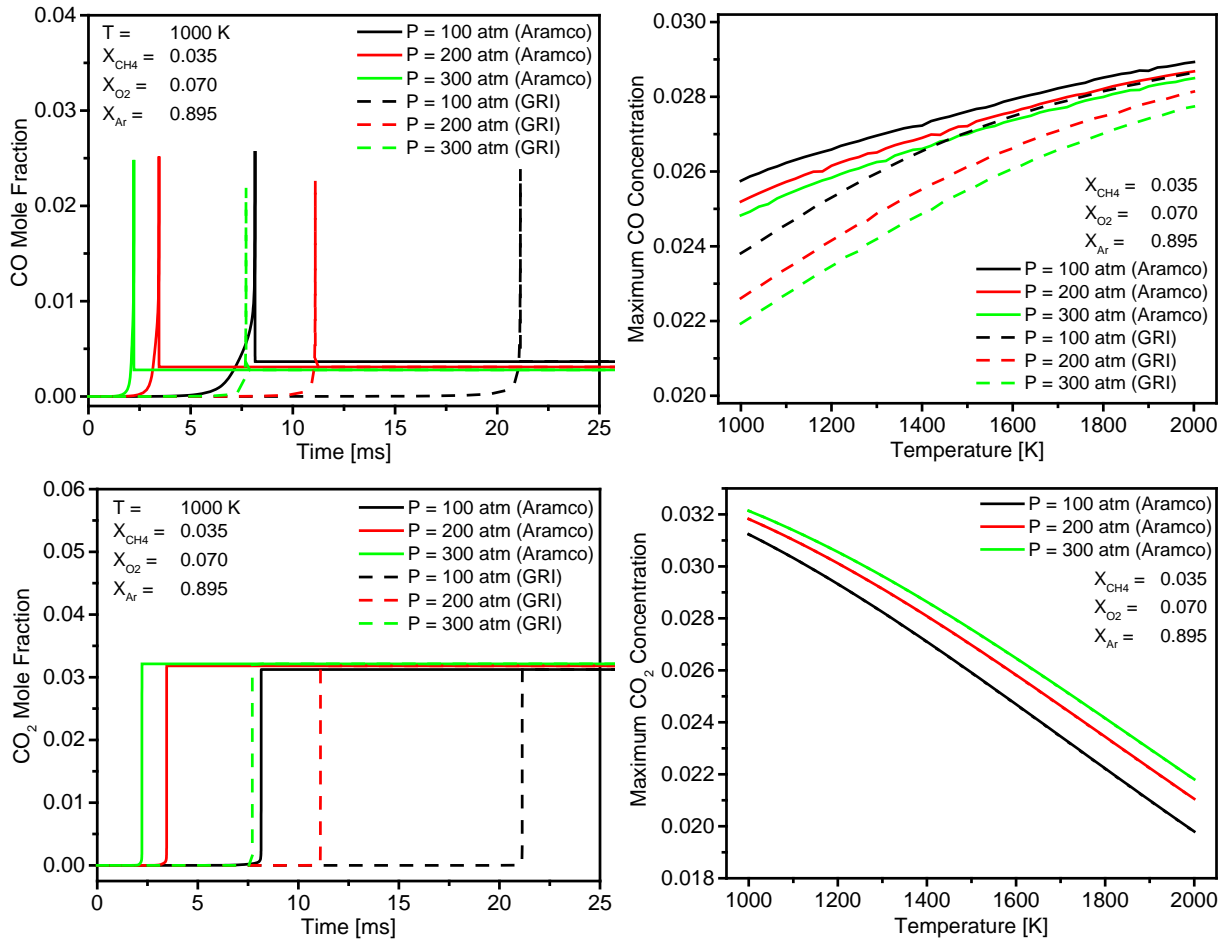


Figure 16: Effect of pressure on carbon monoxide and carbon dioxide concentrations. TOP LEFT: Effect of pressure on carbon monoxide time-histories at 1000 K. TOP RIGHT: Maximum carbon monoxide concentrations at various pressures. BOTTOM LEFT: Effect of pressure on carbon dioxide time-histories at 1000 K. BOTTOM RIGHT: Maximum carbon dioxide concentrations at various pressures. Aramco 1.3 is shown as solid lines and GRI 3.0 as dashed.

Another interesting note from Figure 16 is the differences in the maximum carbon monoxide values compared to the constant carbon dioxide between the two values. Based on the right side of the figure, it shows that the Aramco mechanism predicts 0.2% more carbon monoxide than the GRI mechanism at the lower temperatures. The GRI mechanism also shows a greater reduction with increasing pressure compared to the Aramco mechanism.

Radical formation shows a different trend than the stable species which could help explain the differences between the models at these elevated pressures. For these simulations, three radicals, H, OH and CH, were examined and comparisons have been made between the two species. For both H atoms and OH molecules, the Aramco mechanism predicted higher peak values and overall concentration. CH radicals had higher peaks for the GRI mechanism, although the overall value is lower for CH radicals compared to H and OH. Figure 17 shows the time-histories of the different radicals during combustion. Based on the three graphs on the right side, the Aramco mechanism predicts more H and OH radicals but less CH. This explains why the Aramco mechanism predicts faster ignition delay times at the lowest temperatures since there are more radicals to cause the reactions necessary to cause ignition.

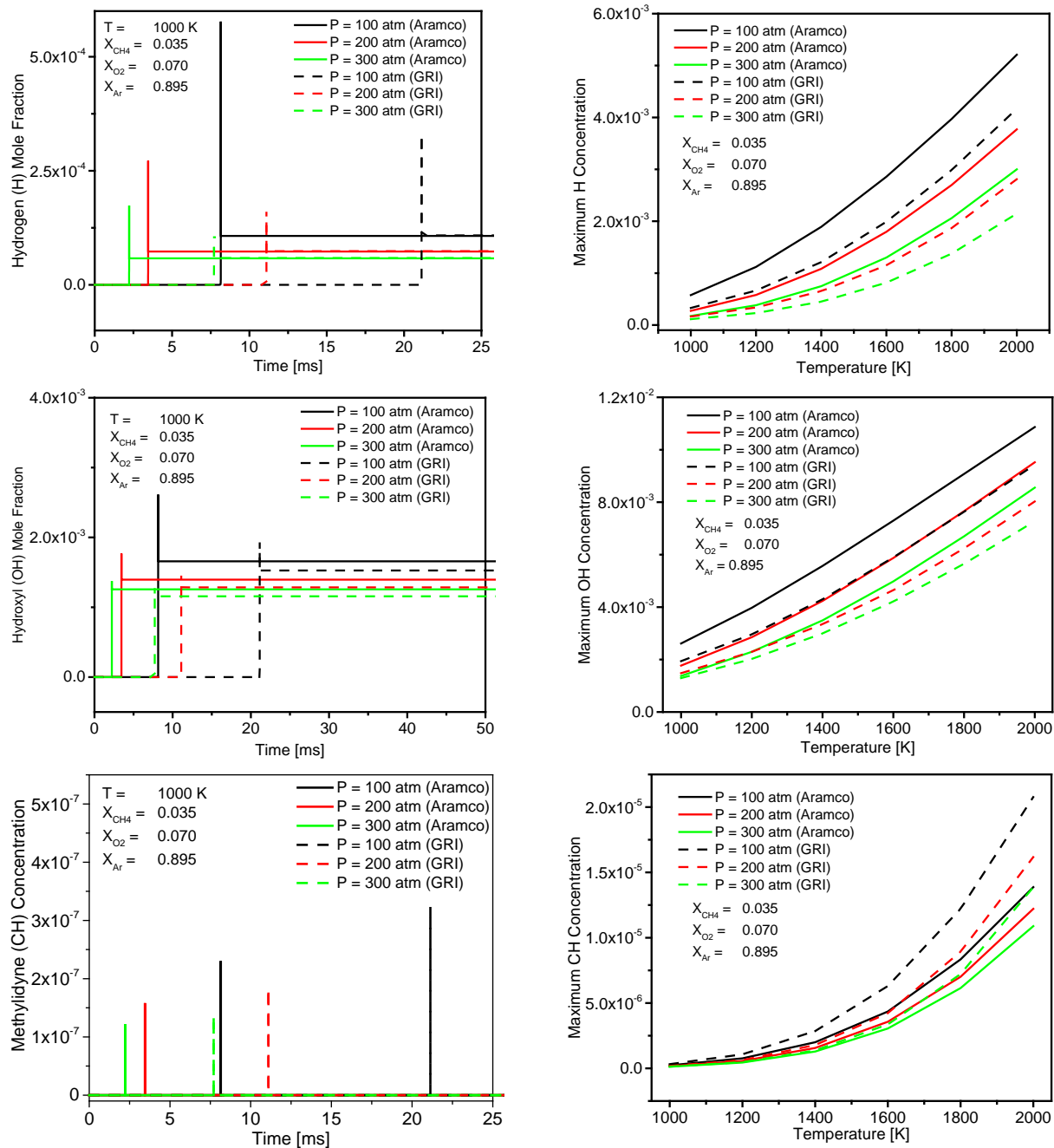


Figure 17: Effect of pressure on the formation of selected radicals. TOP LEFT: H-atom time-histories at $T = 1000\text{ K}$. TOP RIGHT: Maximum H-atom concentrations at various pressures. MIDDLE LEFT: Hydroxyl time-histories at $T = 1000\text{ K}$. MIDDLE RIGHT: Maximum OH concentrations at various pressures. BOTTOM LEFT: Methylidyne (CH) time-histories at $T = 1000\text{ K}$. BOTTOM RIGHT: Maximum CH concentrations at various pressures. Aramco 1.3 is shown as solid lines and GRI 3.0 as dashed.

Effect of Carbon Dioxide Dilution at Low Pressures

Ignition Delay Times

The ignition delay times at low temperatures show similar values between the two different models. Based on Figure 18, it shows that the ignition delay time is increased with increasing carbon dioxide mole fractions. There is also some differences between the two different models with the GRI 3.0 mechanism showing a more linear trend than the Aramco 1.3 mechanism. More importantly, it shows that at these low pressure conditions of more conventional pressures and temperatures the ignition delay time is extremely high. At 10 atm, it approaches 1 s for the lower temperatures that can currently be achieved in a combustor for long durations. The faster ignition events are also extremely hot which means that these types of engines below the supercritical point might be extremely hard to develop.

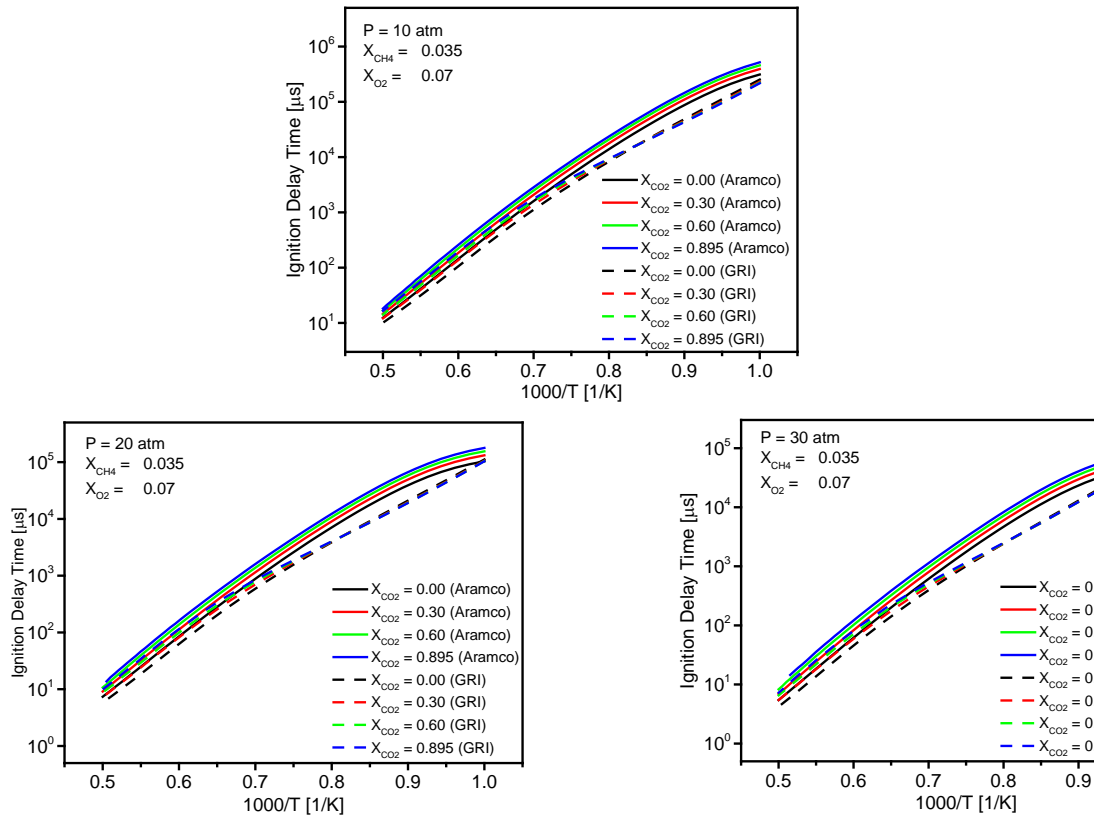


Figure 18: Ignition delay times at low pressures. TOP: Ignition delay times at 10 atm. BOTTOM LEFT: Ignition delay times at 20 atm. BOTTOM RIGHT: Ignition delay times at 30 atm. Aramco 1.3 is shown as solid lines and GRI 3.0 as dashed.

Temperature and Pressure Rise

Temperature and pressure are directly related to the amount of energy released by the combustion event. Figure 19 shows the temperature and pressure rise for various concentrations of carbon dioxide at 10 atm and 1000 K. Both models show that the maximum temperature and pressure are equal for the same conditions. The main difference between the models is that both rises occur slower for the Aramco mechanism. It takes 80 ms to reach the maximum without carbon dioxide and over 300 ms with a mole fraction of $X_{CO_2} = 0.895$. This shows a major underlying difference between the two mechanisms with it showing that the ignition occurs

slower with the Aramco mechanism compared to the other. Understanding the difference between these two mechanisms is important to understanding carbon dioxide diluted mixtures and thus supercritical CO₂ cycles.

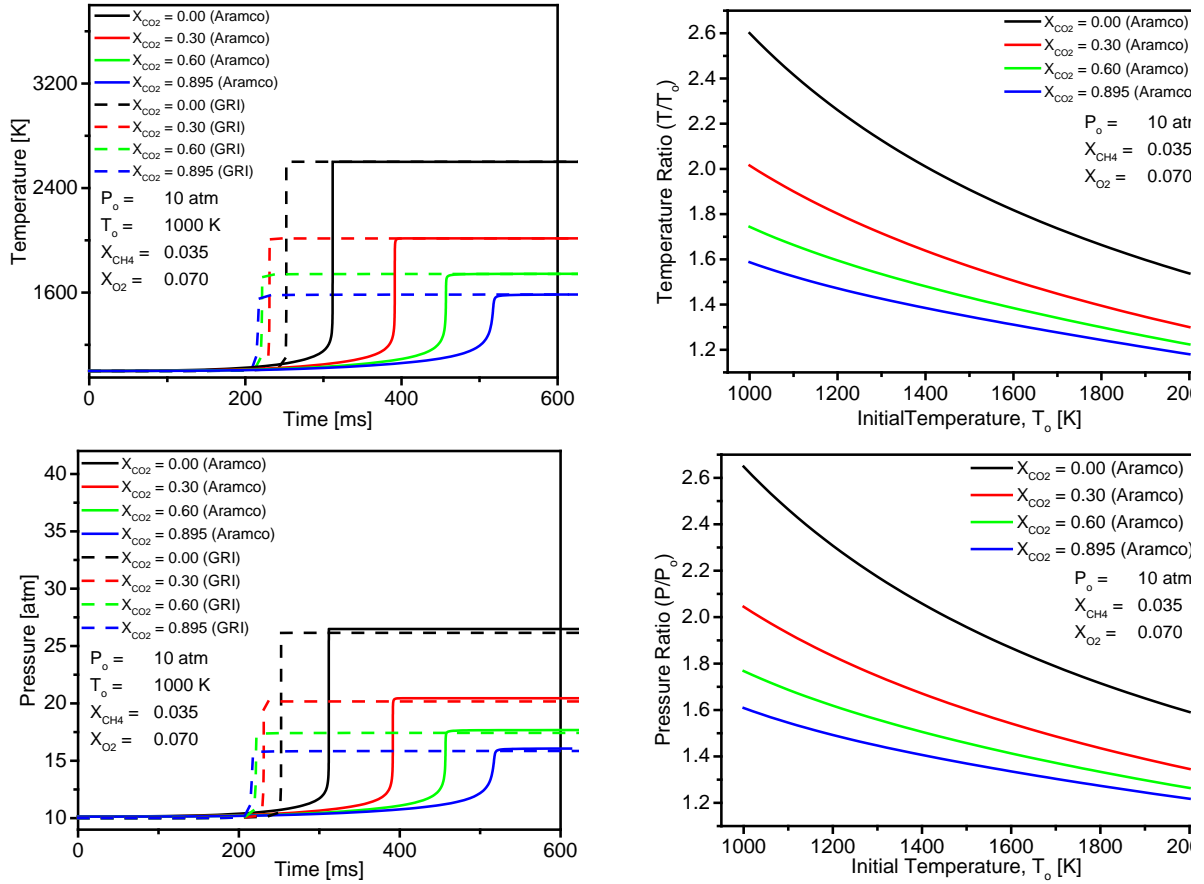


Figure 19: Temperature and Pressure Rise at 10 atm and 1000 K. TOP LEFT: Temperature time-history. TOP RIGHT: Ratio of maximum temperature to initial temperature for various concentrations of carbon dioxide. BOTTOM LEFT: Pressure time-history. BOTTOM RIGHT: Ratio of maximum pressure to initial pressure for various concentrations of carbon dioxide. Aramco 1.3 is shown as solid lines and GRI 3.0 as dashed.

Effect of Carbon Dioxide Dilution at High Pressures

Supercritical carbon dioxide cycles are systems that are heavily diluted with high pressure carbon dioxide. To model these systems, both the Aramco 1.3 mechanism and the GRI 3.0 mechanism were used for a temperature range between 1000 and 2000 K for pressures at 100, 200 and 300 atm. Carbon dioxide increased from 0 to 89.5% with 3.5% CH₄ and 7.0 O₂ for each mixture.

Ignition Delay Times

The ignition delay times for each system were determined by the Chemkin Pro software based on the inflection point of the temperature. According to the models, carbon dioxide does not have a major influence on the ignition delay times instead decreasing the ignition delay time for a similar amount with each increase in carbon dioxide. The Aramco mechanism continues to have the same nonlinear trend using the logarithmic scale. This shows that the simple modeling of a constant for the activation energy may not be possible for these lower temperatures. Both mechanisms also show better agreement with itself for the higher concentrations of carbon dioxide with the GRI showing only slight variation at the higher temperatures for a pressure of 300 atm. Figure 20 shows the ignition delay times vs the inverse of temperature for increasing percentages of carbon dioxide.

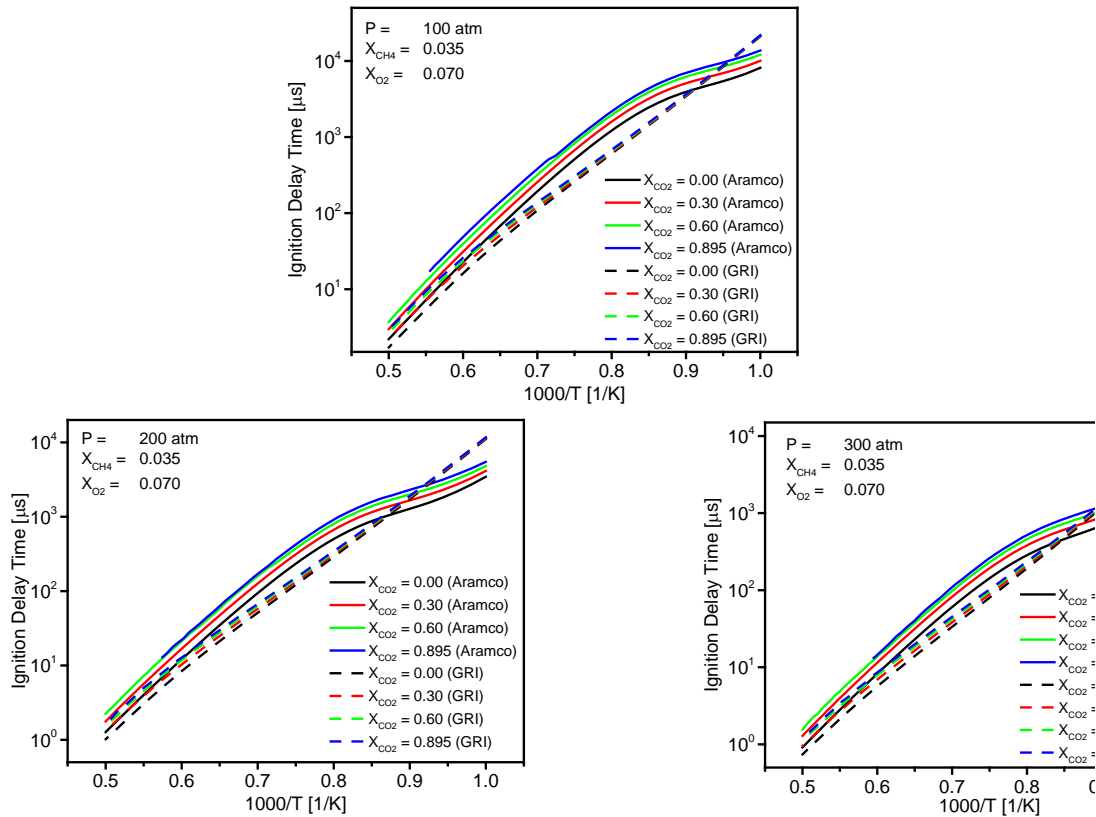


Figure 20: Ignition delay times at high pressures. TOP: Ignition delay times at 100 atm for different levels of carbon dioxide dilution. BOTTOM LEFT: Ignition delay times at 200 atm for different levels of carbon dioxide dilution. BOTTOM RIGHT: Ignition delay times at 300 atm for different levels of carbon dioxide dilution. Aramco 1.3 is shown as solid lines and GRI 3.0 as dashed.

Temperature and Pressure Rise

The turbine inlet conditions are important when designing these advanced power cycles. Therefore understanding how high the temperature and pressure rise during the combustion process is an important part of designing a direct-fired sCO₂ combustor. Therefore the pressure and the temperature time-histories were simulated for initial pressures between 100 and 300 atm. Based on the simulation results, both models predict that the pressure and the temperature will be reduced with increasing carbon dioxide concentrations as shown in Figure 21.

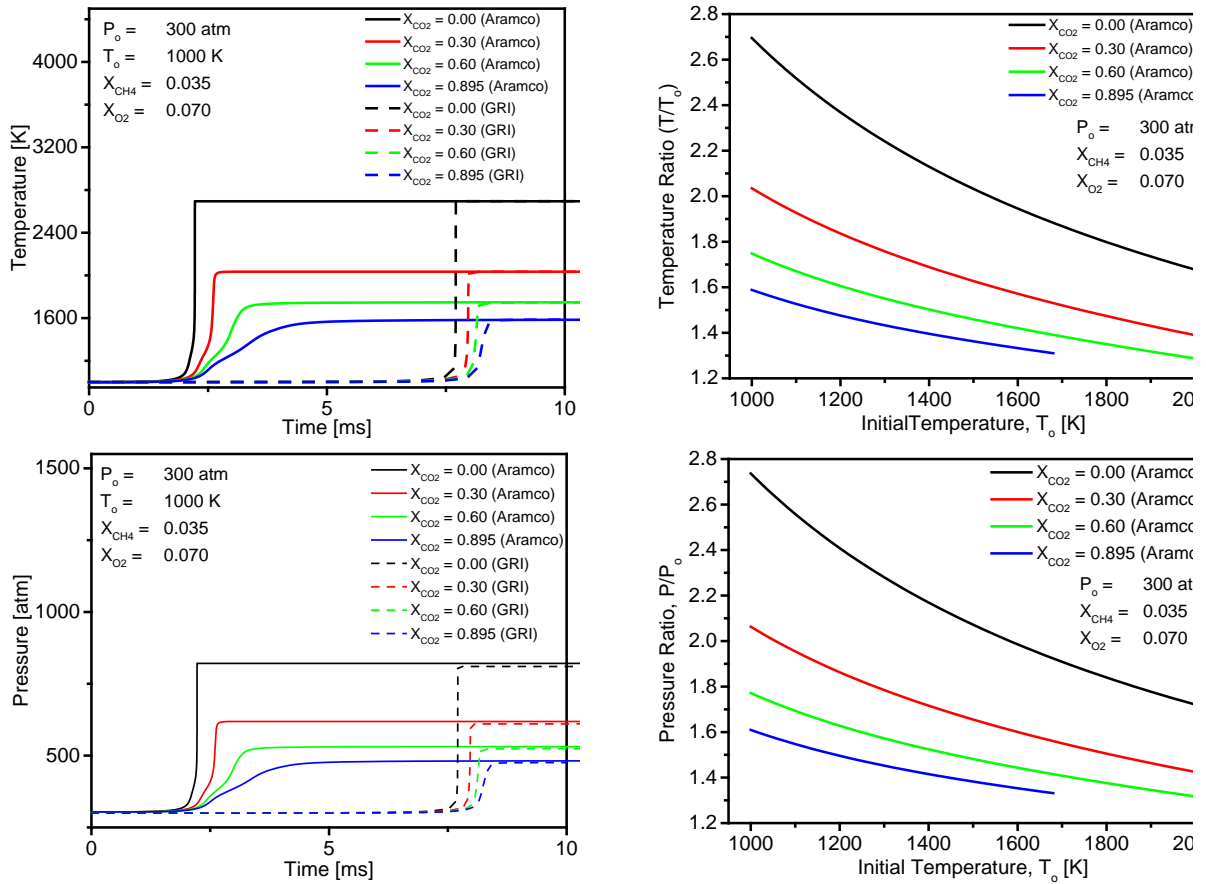


Figure 21: Temperature and Pressure Time-histories at 300 atm and 1000 K. TOP LEFT: Temperature time-history. TOP RIGHT: Ratio of maximum temperature to initial temperature for various concentrations of carbon dioxide. BOTTOM LEFT: Pressure time-history. BOTTOM RIGHT: Ratio of maximum pressure to initial pressure for various concentrations of carbon dioxide. Aramco 1.3 is shown as solid lines and GRI 3.0 as dashed.

This is understandable as carbon dioxide has a higher specific heat and therefore releases less energy compared to an argon diluted mixture. This smaller pressure gain is important as if correct would allow for smaller pressure ratios across the turbine and therefore less power produced by the cycle. Another interesting part of the simulations are that while both mechanisms reach the same final value after combustion, the time that it takes to reach that value is much longer for the Aramco Mechanism and that the time is longer with higher carbon dioxide

dilution. Figure 22 shows the time it takes for the pressure and temperature to reach its final value for both mechanisms.

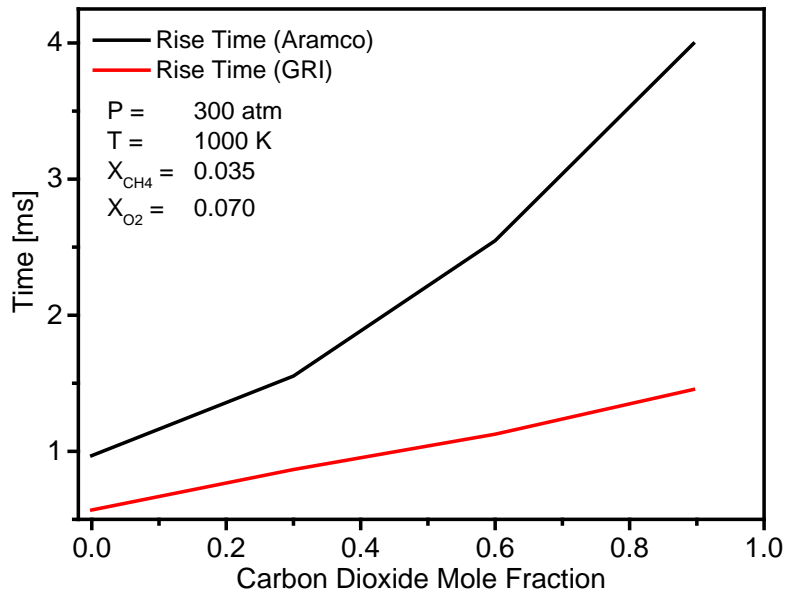


Figure 22: Comparison of Rise Time as a function of carbon dioxide concentration.

Low Fidelity of Models

One of the main issues with using either of the two mechanisms to simulate the combustion process at supercritical conditions is that there is almost no data to validate the mechanisms. Both mechanisms were validated for pressures of 20 atm at the highest levels and were designed for pressures of around 10 atm. The other issue is that the mechanisms were not created with carbon dioxide as the diluent. As a result, the mechanism can only be a rough guide to how such a system will react. A better method would be to develop a new mechanism that incorporates such effects and looks at any possible real gas effects that could also skew the results.

CHAPTER 5: RESULTS AND DISCUSSIONS

Experiments were performed behind reflected shockwaves for temperatures between 1500 and 2200 K. Pressures for these experiments ranged between 0.7 to 9.5 atm. The equivalence ratio of 0.5, 1.0 and 2.0 and the mole fraction of carbon dioxide was 0.0, 0.3, 0.6 and 0.895.

Ignition Delay Time Measurements

Ignition delay times in a shock tube is considered the time between the arrival of the reflected shockwave at the 2 cm location from the end wall and the start of the pressure or emissions rise in the signal. As the pressure and temperature rises is considered to be instantaneous upon the arrival of a shockwave then the pressure and temperature behind the reflected shockwave can be considered to be constant. An example of the ignition delay time can be seen in Figure 1 on the left. Normally, the arrival of the reflected shockwave arrival would be considered to be at the midpoint of the pressure increase but, due to bifurcation of the shockwave, the arrival of the shockwave was considered to be the peak of the absorbance trace for the 3.4 μm laser. This peak, a product of beam steering, is considered to more accurate as it is much more concise compared to the pressure trace. An example of the pressure trace (left) compared to the absorption trace (right) can be seen in Figure 23.

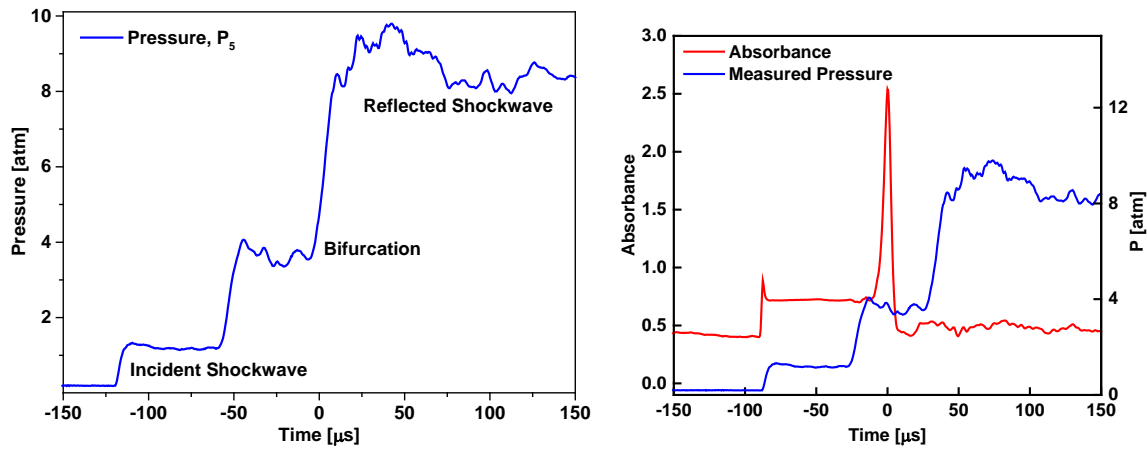


Figure 23: *LEFT: Traditional interpretation of time zero. RIGHT: Time zero based on the interpretation of methane absorption. The time zero for the traditional interpretation is 31 μs later due to the bifurcation of the reflected shockwave compared to the absorption spike on the methane laser.*

The figures show that due to the bifurcation of the shockwave the pressure is no longer a good representation of the start of the test conditions and the laser shows a much clearer time due to the beam steering caused by the shockwave. It also shows that due to bifurcation the time for the arrival of the reflected shockwave becomes difficult to determine resulting in a change of 31 μs in the example above.

Experiments at 1 atm

Experiments were performed at atmospheric pressure for a variety of conditions. Conditions include experiments with no carbon dioxide and several different equivalence ratios. Each experiment that was performed at this pressure is shown in Table 1. These experiments were taken from Koroglu et al. [22]. The conditions for each experiment had a range of temperatures

between 1577 K and 2144 K. There were three different levels for the mole fraction of carbon dioxide (0.0, 0.3, and 0.6) and the equivalence ratio varied between 0.5 and 2.0.

Table 1: Summary of Experimental Data at Atmospheric Pressure

P_5 [atm]	T_5 [K]	X_{CO_2}	X_{CH_4}	X_{O_2}	X_{AR}	Φ	τ [μ s]
0.882	1577						2142.2
0.87	1663						980.5
0.871	1792	0.0	0.035	0.07	0.895	1.0	352.1
0.835	1891						194.9
0.886	2144						38.5
0.818	1737						530.9
0.788	1801						382.3
0.776	1850	0.3	0.035	0.07	0.595	1.0	277.9
0.755	1903						185.2
0.731	1942						157.4
0.684	2022						104
0.814	1714						601.4
0.826	1791						370.8
0.829	1837	0.3	0.0175	0.07	0.6125	0.5	269.5
0.766	1846						262.7
0.725	1877						154.0
0.703	2012						90.3
0.68	1736						758.5
0.716	1812						427.6
0.721	1841						342.9
0.704	1857	0.3	0.07	0.07	0.56	2.0	311.5
0.681	1864						302.7
0.677	1921						190.3
0.615	1962						184.2
0.698	1799						465.9
0.641	1851						330.7
0.603	1960	0.6	0.035	0.07	0.295	1.0	196.4
0.528	2114						92.8
0.567	2091						89.5

The ignition delay times increase with increasing carbon dioxide mole fractions as expected from the chemical kinetic mechanisms. At these low pressures, the ignition delay times show a linear trend when plotted as a logarithmic scale as is expected. Figure 24 shows the ignition delay times

for plotted for the different amounts of carbon dioxide mole fractions (Figure taken from Koroglu et al. [22]). It shows that at atmospheric pressures, there is little difference in the ignition delay times when carbon dioxide is added to the mixture. The difference at the higher temperatures was considered to be approximately 25% compared to the tests without carbon dioxide and 15% at the lower end. The uncertainty of such experiments is considered to be around 20% and therefore the change is within the uncertainty.

The equivalence ratio only has a small effect on the ignition delay time as shown in the right image of Figure 2. It shows that the at an equivalence ratio of 0.5, the ignition delay times are the faster due to an excess of oxygen. The equivalence ratio of 2.0 causes an increase in the ignition delay times as there is more fuel than oxygen needed for the reactions. [Add comment about the percent difference and compare to the uncertainty of the ignition delay times.

The uncertainty in the ignition delay times for these experiments was determined from a combination of the physical sensor used in the experiments and the uncertainty in the pressure and temperature of the region. More discussion on the uncertainty will be discussed later in this chapter.

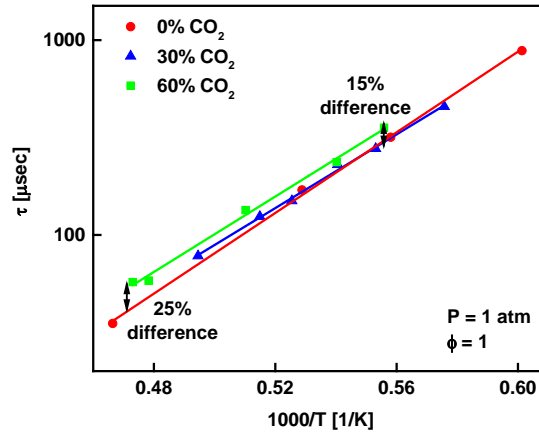


Figure 24: Comparison of Ignition Delay Times measurements for carbon dioxide mole fractions of 0.0, 0.3 and 0.6. Pressure for each experiment was 1 atm and the equivalence ratio was 1.0 [22].

Due to the large uncertainties in the ignition delay times from the emissions trace, a second method was also used to measure the ignition delay time using the 3.4 μm laser and the Beer-Lambert Law (Equation 36) to measure the methane concentration decay times [22]. This method has much smaller uncertainty for the absorption cross-section and mole fraction of ± 4 and $\pm 6\%$, respectively. The method for the uncertainty calculation has been detailed in Koroglu et al. [34]. The methane concentration decay time was therefore considered to be the time it took for the methane mole fraction to be reduced to $1/3^{\text{rd}}$ of its initial value. This method shows similar trends as the ignition delay times but is much more accurate due to the accuracy of the method. Figure 25 shows the difference between the methane concentration decay time and the peak of the normalized CH^* emissions trace. It is shown that the methane decay time can be considered a good method for determining the ignition delay time and is more accurate compared to the standard emissions approach above.

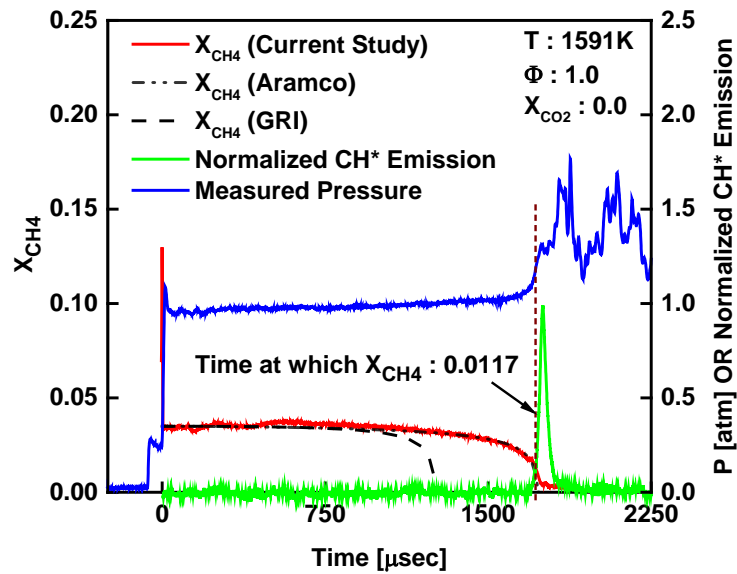


Figure 25: Pressure and CH₄ mole fraction time-histories during the ignition of 3.5% CH₄ and 7% O₂ in argon. The experimental data were obtained at P₅ ~ 1.0 atm and T₅=1591 K [22].

Experiments at 4 atm

Experiments measuring the ignition delay time of carbon dioxide diluted methane mixtures was also performed around 4 atm. These experiments ranged from 1610 K to 1904 K. The equivalence ratio ranged from 0.5 to 2.0. All of the experiments were performed with a carbon dioxide mole fraction of 0.3. All experiments are shown in Table 2 and are taken from Koroglu et al. [22].

Table 2: Summary of Ignition Delay Experiments at 4 atm

P_5 [atm]	T_5 [K]	X_{CO_2}	X_{CH_4}	X_{O_2}	X_{AR}	Φ	τ [μ s]
4.038	1660						363.6
3.929	1706						232.0
3.868	1748						162.2
3.653	1807	0.3	0.035	0.07	0.595	1.0	100.1
3.602	1865						59.9
3.544	1904						38.9
4.104	1610						396.9
4.41	1613						391.7
4.035	1696						169.3
3.688	1760	0.3	0.0175	0.07	0.6125	0.5	105.5
3.722	1848						57.1
3.565	1881						40.5
3.828	1632						535.2
3.562	1677						382.9
3.792	1684						337.9
3.897	1681						323.1
3.462	1736	0.3	0.07	0.07	0.56	2.0	233.9
3.355	1800						121.3
3.418	1884						52.3
3.288	1896						51.9

Compared to the experiments at atmospheric pressures, these experiments show reduced ignition delay times for the same conditions. With an increase in pressure of three atmospheres, the ignition delay times were reduced as was expected by both mechanisms. Another interesting observation is that the difference between the two models has been increased slightly compared to atmospheric pressure. The experimental data also tends to start around the GRI prediction at the higher temperatures before becoming closer to the prediction by the Aramco mechanism. Figure 26 shows the ignition delay times for each condition at the elevated pressures compared to that similar conditions at atmospheric conditions. All experiments are compared to both the GRI 3.0 and Aramco 1.3 mechanisms.

Another interesting note between the different equivalence ratios is that the pressure was reduced with increasing equivalence ratio for both the low and high pressure experiments. The pressure, as determined from the FROSH program had an average of 3.92 atm when the equivalence ratio was 0.5 and decreased to 3.58 atm. There are several possible reasons such as it being a result of slightly different mixtures but it is more likely an energy release difference as the shockwaves had similar velocities at the same temperatures.

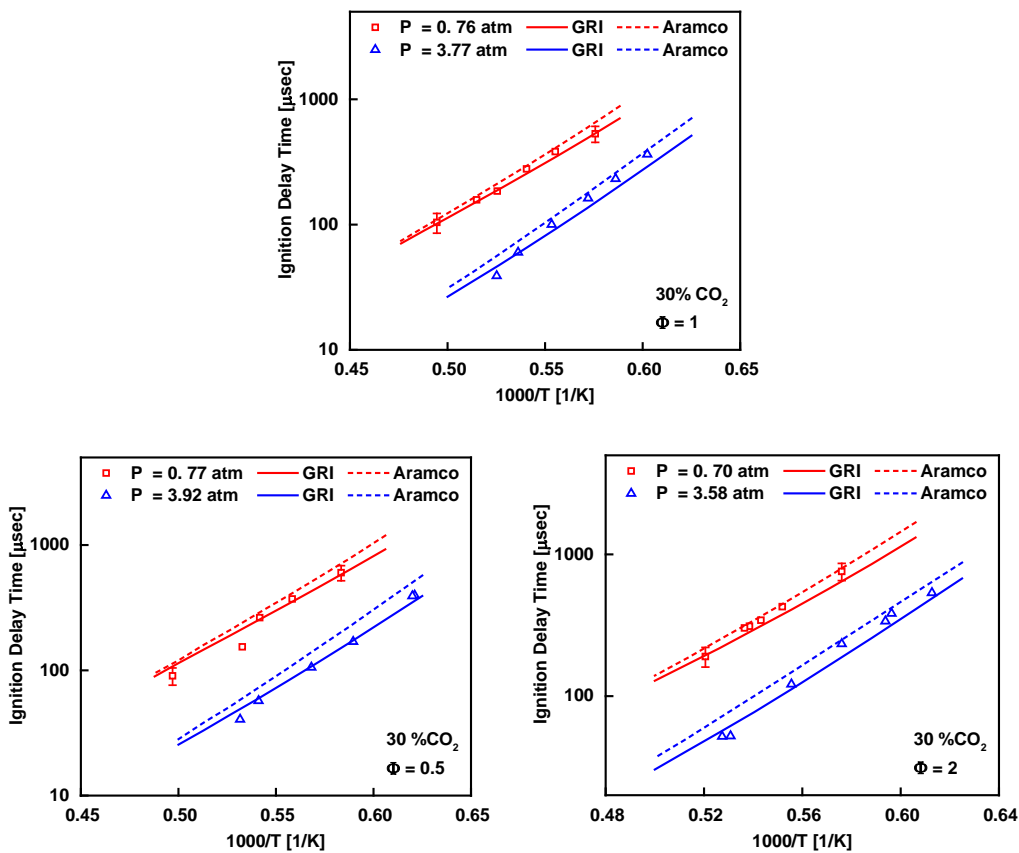


Figure 26: Ignition Delay Times at pressures around 4 atm for different equivalence ratios compared to experiments at atmospheric conditions. TOP: Ignition delay times at an equivalence ratio of 1. MIDDLE: Ignition delay times at an equivalence ratio of 0.5. BOTTOM: Ignition delay times at an equivalence ratio of 2. All experiments are compared to the Aramco and GRI mechanism. Figure was taken from Koroglu et al. [22].

Experiments at 8 atm

The last set of experiments for these experiments were performed around 8 atm for carbon dioxide mole fractions ranging from 0.3 to 0.6. Each experiment performed is shown below in Table 3.

Table 3: Summary of Ignition Delay Experiments at 8 atm.

P₅ [atm]	T₅ [K]	X_{CO2}	X_{CH4}	X_{O2}	X_{AR}	Φ	τ [μs]
8.906	1521						702.0
8.847	1558	0.3	0.035	0.07	0.595	1.0	497.5
8.714	1625						274.5
9.016	1749						105.0
7.418	1568						598.0
7.429	1590						501.5
7.483	1636	0.6	0.035	0.07	0.295	1.0	309.5
6.868	1667						213.5
7.002	1725						151.5
6.974	1764						128.0
7.353	1568						625.5
7.008	1635	0.895	0.035	0.07	0.0	1.0	352.0
6.670	1712						210.5
6.037	1791						143.0

The experiments shows further agreement with the models splitting them for the different experiments. One major difference between the ignition delay times and the models is the less linear trend in the ignition delay times (although it would still be within the bounds of the uncertainty). Figure 27 shows the ignition delay times for the two sets of experiments and the comparison to the models.

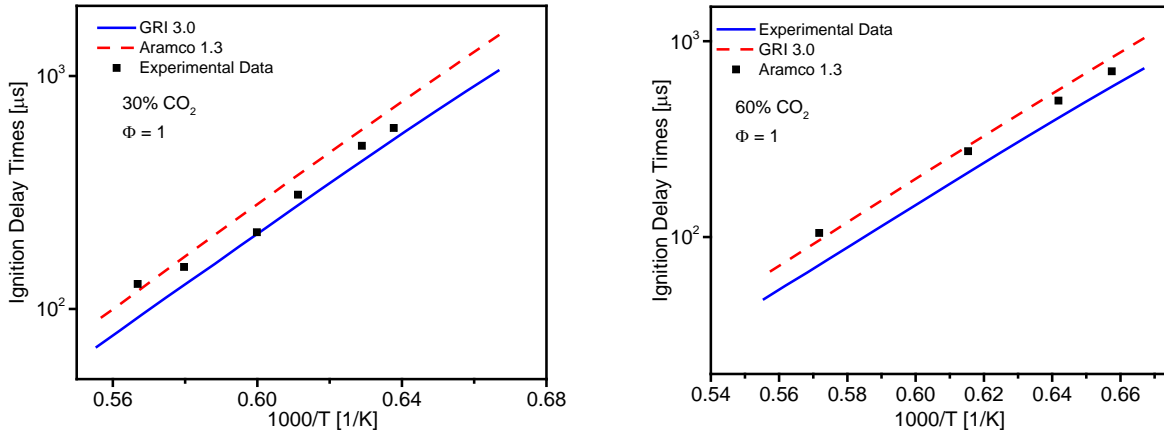


Figure 27: Ignition delay times at 8 atm. LEFT: Ignition delay times with 30% carbon dioxide. RIGHT: Ignition delay times at 60% carbon dioxide. All experiments are compared to the Aramco and GRI mechanism.

Unfortunately it is hard to compare the two different mixtures to each other due to the large pressure difference seen at these conditions. The average pressure for a mole fraction of 0.3 was 8.871 atm and the average pressure for a mole fraction of 0.6 was 7.196 atm. This difference of almost two atmospheres does not allow for a great comparison. Another issue that was seen at these pressure was the reduced test time. The test time for these mixtures was less than 700 μs which limited the range of temperatures that could be measured. Each group had an approximate window of 200 K that could be measured due to this reduced test time.

Ignition Delay Time Correlation

A correlation was created to predict the ignition delay times using a modified Arrhenius format (Equation 37). Equation 38 shows the correlation between the measured ignition delay times and the pressure, temperature, methane concentration, oxygen concentration and carbon dioxide

concentration. The activation energy was determined to be 47539.6 cal/mol with an uncertainty of ± 542 cal/mol.

$$\tau_{ign} = A \exp\left(\frac{E}{RT}\right) P^b \phi^c [CH_4]^d (1-[CO_2])^e \quad (37)$$

$$\tau_{ign} = 0.032 \exp\left(\frac{47539.6}{RT}\right) P^{-0.74} \phi^{-1.02} [CH_4]^{1.24} (1-[CO_2])^{-0.13} \quad (38)$$

Alternative Methods for measuring the ignition delay time

Several different methods were considered for measuring the ignition delay time for the different experiments. The first method was to use the maximum of the emissions trace as the time of ignition. This was determined by normalizing the emissions trace and then determining the point at which it reaches 1. There are several arguments that ignition occurs only when there are a significant number of radicals present for reactions to occur. The peak value of the emissions would give that value for these experiments. The second method was to determine the sharpest rise of emissions (normally around the halfway mark) and then to draw the tangent line at this point. The location that this tangent line intersects the baseline is then determined to be the ignition delay time. This method is based on the start of the decomposition of the fuel and often corresponds with the rise in pressure. A third method was to measure the midpoint of the emissions trace as the ignition delay time. It was considered a compromise between the radical build up and decomposition.

The method used above was the peak of the emissions trace. This method was chosen due to its similarity with the zero point of methane. Generally, ignition does not occur until the fuel

decomposes and it gives us the best agreement with these results. This method also showed better agreement with the predictions. Each method is shown in Figure 28 and compared to both the GRI and the Aramco mechanisms.

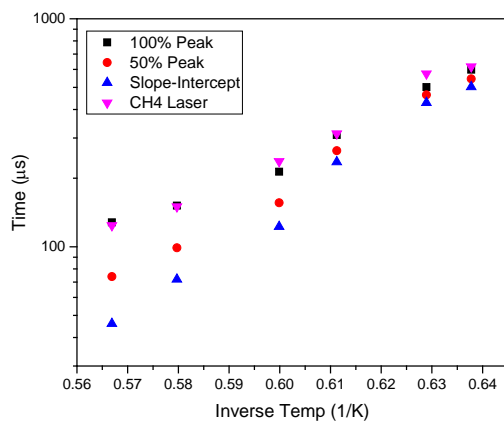


Figure 28: Comparisons of Different Methods of Ignition Delay Time Measurements. It shows that as the ignition delay times get smaller, the difference between the different methods become increasingly relevant.

Bifurcation of Shockwave

Bifurcation is a major concern for the experiments presented above and leads to uncertainty in the experiments. When the shockwave reflects from the end wall, the normal shockwave splits due to the boundary layer forming two opposing oblique shocks, or a lambda wave. The lambda wave is formed due to the boundary layer separating from the end wall. This phenomenon occurs primarily due to the lack of momentum in the boundary layer to pass through the normal shockwave as described by Mark [35]. Figure 29 shows the image of a bifurcated shockwave and the different regions that are created.

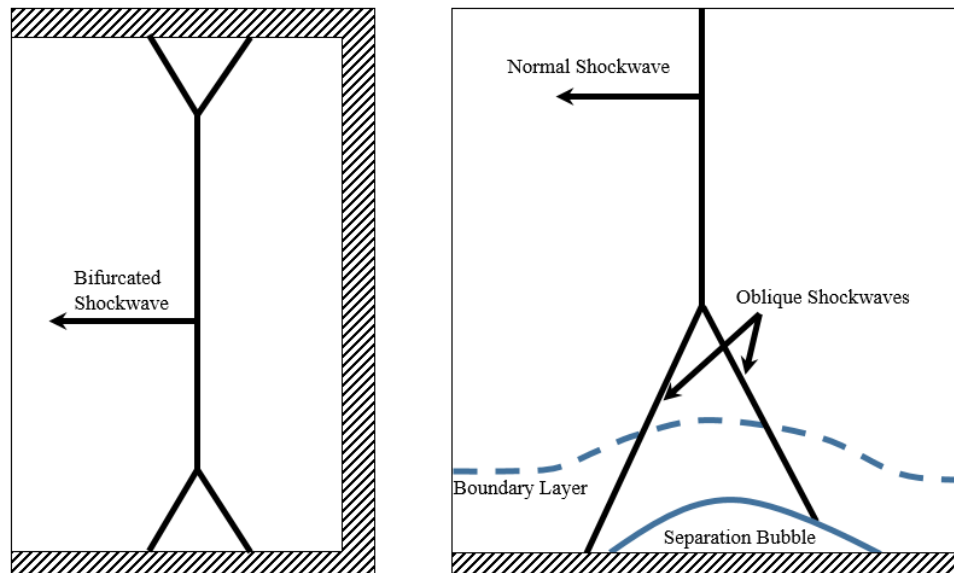


Figure 29: Example of Bifurcation of Reflected Shockwave.

The bifurcation of the shockwave occurs as a result of the composition of the gases. Monoatomic gases such as argon do not have bifurcation as the boundary layers are not considered energy deficient but diatomic molecules and polyatomic molecules such as was added in the above experiments can cause bifurcation.

The effects of bifurcation have been well documented from many different studies [36-43]. The main effects of bifurcation in carbon dioxide mixtures were also explained by Hargis and Petersen [21]. These works explained the non-steady conditions that are often seen in the reflected shock region and how temperature, pressure and mixture composition effect the experiment. One major concern that is described by Nowak et al., is the formation of hot spots near the wall [43]. These events that are caused by the swirling turbulence of the oblique shockwaves can cause early and heterogeneous ignition resulting in a poor understanding of the shock conditions before ignition. This is also a concern for longer ignition experiments as the test conditions present become increasingly unstable and early ignition more likely.

With the addition of carbon dioxide, bifurcation effects become increasingly important. Hargis and Petersen explored the pressure overshoot time and how it increases with increasing amounts of carbon dioxide [21]. This time means that the bifurcation was larger and therefore the turbulence and pressure, temperature would become increasingly uncertain. The temperature was also considered in the same paper and it was determined to have little effect on the bifurcation compared to the carbon dioxide concentration.

Other Non-idealities

There are also several other concerns besides bifurcation that were considered when analyzing the results from the experiments. The first is an indirect effect of carbon dioxide and bifurcation on the pressure in the test mixture. Others include the energy released during ignition and effects on the diaphragm opening.

It was noticed during these experiments that the calculated pressure and the measured pressure were not always matching each other with the calculated pressure being as high as 20% less than the measured pressure before the experiments. Several theories were considered for the differences, and it was determined that the addition of carbon dioxide in the mixture increased the discrepancy and minor increases with increasing pressure. Figure 30 shows the calculated pressure as a percentage of the measured pressure for the different mixtures and for several argon baseline shocks.

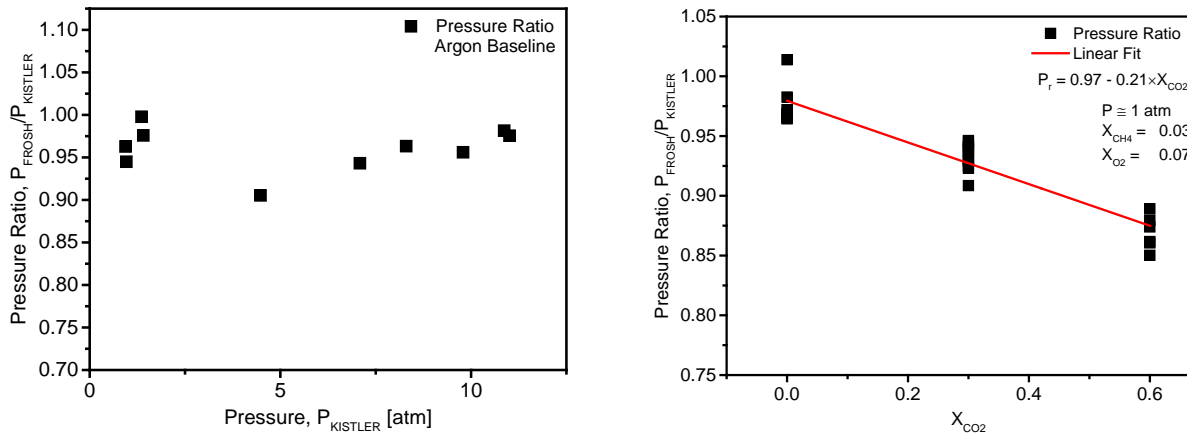


Figure 30: Comparison of the measured pressure to the calculated pressure. LEFT: Pressure Ratio of Frosh to Kistler for Argon Baselines at various pressures. RIGHT: Pressure Ratio of Frosh to Kistler during methane oxidation at various concentrations of carbon dioxide for 1 atm.

It is shown that the Argon baseline and the non-diluted mixtures had better agreement in the calculated pressure and the measured pressure with calculated pressures being at least 97% of the measured pressure. The most likely result in the difference in the pressures is the effects of bifurcation at the turbulent vortices that are shed from the oblique waves. Since the pressure was measured at the sidewall location for each experiment, it is understandable that this location would be effected by such events that have been described in the literature on bifurcation [40, 43].

This is a concern as the temperature and the uncertainties were calculated based on shock velocity and was independent of the measured pressure. A quick analysis using the equations discussed in Chapter 2 shows that if the measured pressure is used instead of the shock velocity to calculate the temperature, it could increase by 100 K.

Another concern is the decrease in energy released from the higher carbon dioxide mixtures. Carbon dioxide has a high specific heat compared to other gases such as argon or nitrogen. This

higher specific heat causes the temperature and pressure rise to be reduced for the same conditions. As the pressure trace is often used to compare and validate the emissions trace for the ignition delay times, this smaller energy release results in smaller and sometimes negligible pressure rises that result in less verification in the pressure trace. This is overcome for these experiments using the methane laser absorption that can also measure the ignition delay time in the experiments. This phenomenon was noted in Koroglu et al. [22].

The physical formation of the shockwave can also lead to non-ideal conditions for the experiments. The diaphragm was ruptured using a four-sided cutter that has been shown to produce consistent pressures at the test section [22, 27, 44]. Although the pressures have been shown to be consistent, there are still several possible issues that can present themselves. The first issue is that the formation of a shockwave that is not normal or at the desired velocity. A minimum of ten diameters is needed for the proper formation of the shockwave and the shock tube at the university has a length to diameter ratio of 60. More concerning is the diaphragm not being considered an instantaneous rupture. Rupture times for shock tubes are considered to be on the scale of 1 ms [insert citation]. The problem is that the ideal case is for an instantaneous rupture which would result in a perfect shockwave. Through observations, it has been noted that when the final pressure is less than expected, the shockwave is slower than the pressure ratio in the shock tube should have been. This is caused by a slower diaphragm opening and therefore a reduction in the strength of the shockwave. Currently, there has not been a method to predict these weaker shockwaves but the occurrence is rare and therefore can be removed or accounted for in the experiments.

CHAPTER 6: CONCLUSION

Experiments on the effect of carbon dioxide dilution on methane oxidation has been examined behind reflected shockwaves. Experiments were performed at three different pressures for temperatures between 1600 and 2000 K. Three different equivalence ratios and four different concentrations of carbon dioxide were explored.

It has been shown that the ignition delay times and the methane decay time increases with increasing concentration of carbon dioxide. It shows that for mixtures designed for supercritical carbon dioxide, the ignition delay time is will be longer than for more traditional methane cycles. Another important finding from the research is that at the lower pressures tested so far, the current state-of-the-art mechanisms are capable of predicting the ignition delay time reasonably well. This is important as it means that at carbon dioxide does not change the reaction mechanisms drastically at these conditions. It still remains to be seen if this is the same at higher pressures more representative of supercritical cycles.

These results allow for better understanding of the effects of carbon dioxide diluted cycles. As the containment of greenhouse cases and pollutants become increasingly important, it is necessary to understand the effects of carbon dioxide as a diluent. This work starts from the atmospheric pressure and looks at the effects at low pressures to provide data on how carbon dioxide effects the reactions. Using this data, a chemical kinetic mechanism can be created that incorporates carbon dioxide and is validated for pressures from 1 to 300 atm.

In order to create a chemical kinetic mechanism, data is needed for validation. Future experiments should focus on the measuring the ignition delay time at higher pressures.

REFERENCES

- [1] J. Pires, F. Martins, M. Alvim-Ferraz, M. Simões, *Chemical Engineering Research and Design*, 89 (2011) 1446-1460.
- [2] V. Dostal, P. Hejzlar, M.J. Driscoll, *Nuclear technology*, 154 (2006) 283-301.
- [3] J. Gibbins, H. Chalmers, *Energy Policy*, 36 (2008) 4317-4322.
- [4] A. McClung, K. Brun, L. Chordia, in: *The 4th International Symposium - Supercritical CO2 Power Cycles*, Pittsburg, Pennsylvania, 2014.
- [5] R. Allam, J. Fetvedt, B. Forrest, D. Freed, in: *ASME Turbo Expo 2014: Turbine Technical Conference and Exposition*, American Society of Mechanical Engineers, 2014, pp. V03BT36A016-V003BT036A016.
- [6] A.E. Outlook, US Energy Information Administration, *Early Release Overview*, (2014).
- [7] L. Tan, M. Anderson, D. Taylor, T.R. Allen, *Corrosion Science*, 53 (2011) 3273-3280.
- [8] F. Rouillard, G. Moine, F. Charton, in: *CORROSION 2010*, NACE International, 2010.
- [9] V. Firouzdor, K. Sridharan, G. Cao, M. Anderson, T. Allen, *Corrosion Science*, 69 (2013) 281-291.
- [10] S.R. Pidaparti, J.A. McFarland, M.M. Mikhaeil, M.H. Anderson, D. Ranjan, *Journal of Nuclear Engineering and Radiation Science*, 1 (2015) 031001.
- [11] A. Harvey, M. Huber, A. Laesecke, C.D. Muzny, R. Perkins, in: *Southwest Research Institute: The 4th International Symposium–Supercritical CO2 Power Cycles*, 2014.
- [12] B.L. Ridens, K. Brun, in: *The 4th International Symposium - Supercritical CO2 Power Cycles*, Pittsburg, Pennsylvania, 2014.
- [13] A.A. Konnov, I.V. Dyakov, *Experimental thermal and fluid science*, 29 (2005) 901-907.
- [14] S. de Persis, F. Foucher, L. Pillier, V. Osorio, I. Gökalp, *Energy*, 55 (2013) 1055-1066.
- [15] S.p.d. Persis, G. Cabot, L. Pillier, I. Gökalp, A.M. Boukhalfa, *Energy and Fuels*, (2012).
- [16] A. Mazas, D.A. Lacoste, T. Schuller, in: *ASME Turbo Expo 2010: Power for Land, Sea, and Air*, American Society of Mechanical Engineers, 2010, pp. 411-421.
- [17] P. Heil, D. Toporov, M. Förster, R. Kneer, *Proc. Combust. Inst.*, 33 (2011) 3407-3413.

- [18] F. Liu, H. Guo, G.J. Smallwood, *Combustion and Flame*, 133 (2003) 495-497.
- [19] M. Holton, P. Gokulakrishnan, M. Klassen, R. Roby, G. Jackson, *Journal of Engineering for Gas Turbines and Power*, 132 (2010) 091502.
- [20] S.S. Vasu, D.F. Davidson, R.K. Hanson, *Energy & Fuels*, 25 (2011) 990-997.
- [21] J.W. Hargis, E.L. Petersen, *Energy & Fuels*, 29 (2015) 7712-7726.
- [22] B. Koroglu, O.M. Pryor, J. Lopez, L. Nash, S.S. Vasu, *Combustion and flame*, (2015).
- [23] G.P. Smith, D.M. Golden, M. Frenklach, N.W. Moriarty, B. Eiteneer, M. Goldenberg, C.T. Bowman, R.K. Hanson, S. Song, W.C. Gardiner Jr, in, 1999.
- [24] W.K. Metcalfe, S.M. Burke, S.S. Ahmed, H.J. Curran, *International Journal of Chemical Kinetics*, 45 (2013) 638-675.
- [25] C.T. Johansen, in.
- [26] M. Nishida, G. Ben-Dor, O. Igra, T. Elperin, Chapter 4.1 - Shocktubes and Tunnels: Facilities, Instrumentation and Techniques, in: G. Ben-Dor, O. Igra, T. Elperin (Eds.) *Handbook of Shock Waves*, Three Volume Set, Academic Press, 2001.
- [27] B. Koroglu, O. Pryor, J. Lopez, L. Nash, S. Vasu, in: 51st AIAA/SAE/ASEE Joint Propulsion Conference, 2015, pp. 4088.
- [28] K. Batikan, O.M. Pryor, J. Lopez, L. Nash, S.S. Vasu, *Journal of Quantitative Spectroscopy and Radiative Transfer*, in review (2015).
- [29] P.R. Bevington, D.K. Robinson, McGraw-Hill, New York, (2003).
- [30] S.H. Pyun, J. Cho, D.F. Davidson, R.K. Hanson, *Measurement Science and Technology*, 22 (2011) 025303.
- [31] S.H. Pyun, W. Ren, D.F. Davidson, R.K. Hanson, *Fuel*, 108 (2013) 557-564.
- [32] K.-Y. Lam, W. Ren, S.H. Pyun, A. Farooq, D.F. Davidson, R.K. Hanson, *Proc. Combust. Inst.*, 34 (2013) 607-615.
- [33] A.S. Pine, *The Journal of Chemical Physics*, 97 (1992) 773-785.
- [34] B. Koroğlu, Z. Loparo, J. Nath, R.E. Peale, S.S. Vasu, *Journal of Quantitative Spectroscopy and Radiative Transfer*, 152 (2015) 107-113.
- [35] H. Mark, *The interaction of a reflected shock wave with the boundary layer in a shock tube*, National Advisory Committee for Aeronautics, 1958.

- [36] D. Bull, D. Edwards, *AIAA Journal*, 6 (1968) 1549-1555.
- [37] L. Davies, J. Wilson, *Physics of Fluids* (1958-1988), 12 (1969) I-37-I-43.
- [38] V. Fokeev, L. Gvozdeva, in: *Current topics in shock waves 17th international symposium on shock waves and shock tubes*, AIP Publishing, 1990, pp. 862-866.
- [39] G.J. Wilson, S.P. Sharma, W.D. Gillespie, in: *31st AIAA Aerospace Sciences Meeting and Exhibit*, 1993.
- [40] H. Kleine, V. Lyakhov, L. Gvozdeva, H. Grönig, *Bifurcation of a reflected shock wave in a shock tube*, in: *Shock Waves*, Springer, 1992, pp. 261-266.
- [41] M. Ihme, Y. Sun, R. Deiterding, *AIAA Paper*, 538 (2013) 1-14.
- [42] H. Yamashita, J. Kasahara, Y. Sugiyama, A. Matsuo, *Combustion and flame*, 159 (2012) 2954-2966.
- [43] P. Andrzej J. Nowak, M. Lamnaouer, A. Kassab, E. Divo, N. Polley, R. Garza-Urquiza, E. Petersen, *International Journal of Numerical Methods for Heat & Fluid Flow*, 24 (2014) 873-890.
- [44] B. Koroglu, O. Pryor, J. Lopez, L. Nash, S. Vasu, *Proceedings of the 52nd Joint Propulsions Conference*, (2015).